

THESIS FOR THE DEGREE OF LICENTIATE OF ENGINEERING

**Development of a Free Surface Capability in a RANS Solver
with Coupled Equations and Overset Grids**

MICHał ORYCH



Department of Shipping and Marine Technology
CHALMERS UNIVERSITY OF TECHNOLOGY
Göteborg, Sweden 2013

Development of a Free Surface Capability in a RANS Solver with Coupled Equations and Overset Grids

MICHAŁ ORYCH

© MICHAŁ ORYCH

ISSN 1652-9189
Report No 13:145

Department of Shipping and Marine Technology
Chalmers University of Technology
SE-412 96 Gothenburg
Sweden
Telephone + 46 (0)31-772 1000

Printed by Chalmers Reproservice
Gothenburg, Sweden 2013

Development of a Free Surface Capability in a RANS Solver with Coupled Equations and Overset Grids

MICHAŁ ORYCH

Department of Shipping and Marine Technology
Chalmers University of Technology

ABSTRACT

This thesis is a result of investigations carried out during the implementation of a free surface capturing method in a RANS solver. The work consists of two distinct parts which complement each other, and the purpose is to improve the free surface interface sharpness and to reduce numerical diffusion of the gravity waves. The first part deals with numerical schemes and the second with local grid refinement and adaptivity near the interface. There is a vast amount of discretization schemes for convection equations. However, only a subset is found to be applicable to the water fraction transport equation. Here we investigate the performance of selected schemes applied to hydrodynamic problems. Moreover, an additional scheme is developed based on the experience gained during the work. This part of the work was carried out since there is very little information in the literature for problems beyond academic test cases such as bubble convection or two dimensional shape translation and rotation. The second part of the presented work concerns air-water interface refinements using fixed and adaptive overlapping grids. The adaptive refinement grid follows approximately the free surface interface and reduces the refinement thickness, thus reducing the required number of discretization cells. The grid alignment with the interface reduces further the diffusion of the water fraction in the transition region from air to water. The method is validated on 2D and 3D cases. The Duncan submerged hydrofoil test case as well as Wigley, Series 60 and KCS hulls are compared with experiments. A grid dependence study is presented for Wigley and KCS which shows that the code is robust and the deviations from the measurement data are within the expected accuracy of a CFD code for naval applications.

Keywords: RANS; free-surface; overset.

ACKNOWLEDGEMENTS

I would like to express my greatest appreciation to the supervisor of this project Professor Lars Larsson for his constant support and encouragement.

Special thanks should be given to Björn Regnström, the second supervisor, for the first class technical assistance and help with the code.

Finally, I wish to thank Leif Broberg and Magnus Östberg for their help throughout the project.

I would also like to thank my employer FLOWTECH International AB for giving me the opportunity and time to carry out this research work.

CONTENTS

ABSTRACT.....	iii
ACKNOWLEDGEMENTS.....	v
Nomenclature.....	ix
Abbreviations.....	x
1 INTRODUCTION.....	1
1.1 Motivation.....	1
1.2 Background.....	1
1.3 Present Contributions.....	2
1.4 Structure of the thesis.....	3
2 MATHEMATICAL MODEL.....	5
2.1 Introduction.....	5
2.2 Flow equations.....	5
2.3 Interface capturing method.....	6
2.4 Turbulence model.....	6
2.5 Boundary conditions.....	6
3 NUMERICAL METHOD.....	9
3.1 Governing equations in vector form.....	9
3.2 Discretization.....	10
3.2.1 Convection term.....	10
3.2.2 Roe fluxes.....	10
3.2.3 Eigensystem.....	11
3.2.4 First order upwind formulation.....	12
3.2.5 Second order formulation.....	13
3.3 Flux limiters.....	14
3.3.1 Normalised Variable Diagram.....	14
3.3.2 Common schemes for convection.....	17
3.4 Diffusion terms.....	21
3.5 Gravity source term.....	21
3.6 Initial and Boundary conditions.....	22
3.7 Solution Algorithm.....	23
4 ADAPTIVE OVERLAPPING GRID REFINEMENT.....	25
5 CASE STUDIES.....	29
5.1 Submerged hydrofoil test case.....	29
5.1.1 Case description.....	29
5.1.2 Computational setup.....	29
5.1.3 Effects of discretization scheme.....	31
5.1.4 Effects of overlapping refinement	33
5.2 Series 60 test case.....	34
5.2.1 Computational setup.....	34
5.2.2 Effects of discretization scheme.....	35
5.2.3 Effects of overlapping refinement	37
5.3 Wigley test case.....	39
5.3.1 Computational setup.....	40
5.3.2 Results – resistance.....	40
5.3.3 Results – wave pattern.....	43

5.4 KRISO Container Ship test case.....	44
5.4.1 Computational setup.....	44
5.4.2 Results – resistance	46
5.4.3 Results – wave pattern.....	47
6 Conclusions and future work.....	51
REFERENCES.....	52

NOMENCLATURE

A, A_1, A_2	Discrete Jacobian
Fn	Froude number
f, g, h	Convective fluxes
f_v, g_v, h_v	Viscous fluxes
k	Turbulent kinetic energy
L, R	Left and right eigenvectors of A
n_i	Normal to surface
p	Time average pressure
Q	Primitive variable vector
R_i	Volume force
Rn	Reynolds number
t	Time
u_i, u, v, w	Time average velocity components in Cartesian directions
x_i, x, y, z	Cartesian coordinates
α	Volume fraction
ϵ	Dissipation of turbulent kinetic energy
λ	Eigenvalues of A
μ	Dynamic viscosity
μ_T	Turbulent dynamic viscosity
τ_{ij}	Stress tensor
ν	Kinematic viscosity, μ/ρ
ν_T	Turbulent kinematic viscosity, μ_T/ρ
ν_E	Total kinematic viscosity, $\nu + \nu_T$
ϕ	General variable
ρ	Density
σ_{ij}	Total stress tensor
ξ_B	Parameter direction crossing the boundary
ω	Specific dissipation of turbulent kinetic energy

ABBREVIATIONS

ADI	Alternating Direction Implicit
CBC	Convection Boundedness Criteria
CFD	Computational Fluid Dynamics
FVM	Finite-Volume Method
KRISO	Korean Research Institute of Ships and Ocean Engineering
Lpp	Length between perpendiculars
NVD	Normalised Variable Diagram
RANS	Reynolds Averaged Navier-Stokes
TVD	Total Variation Diminishing
VOF	Volume of Fluid

1 INTRODUCTION

1.1 Motivation

In the design process of ships an accurate assessment of forces acting on the hull in motion is of a great importance. Nowadays model tests in towing tanks still play the major role in this process. However, an interest in the Computational Fluid Dynamics (CFD) tools for designers is growing steadily since the first commercial methods were introduced over 20 years ago. The numerical codes become more and more accurate and robust. Maybe it will take another 20 years until the physical tests are obsolete for routine applications, such as required power prediction or manoeuvring performance, but we can already get great support from CFD as a complement to the model tests. The field of aero- and hydrodynamics of ships can be illustrated as a combination of theory, experimental and CFD methods supporting each other, see Figure 1.

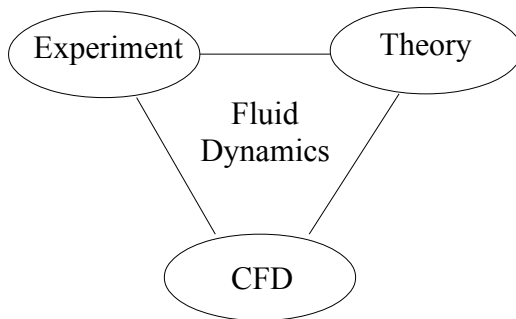


Figure 1: General picture of fluid dynamic field.

Numerical predictions are helpful in an early assessment of ship performance already at the design stage. Also, as a complement to the model basin they can reduce the number of tests or give an excellent guidance on what cases are most interesting to investigate. CFD gives an opportunity to explore novel solutions and stimulate progress in ship developments with reduced cost compared to the tests.

The main goal of the following work is the further development of an easy to use CFD tool for ship designers and includes introduction of a free-surface capturing capability.

1.2 Background

During the last two decades computational fluid dynamics (CFD) has been used for various applications in naval architecture and it has become a valuable tool for ship designers. The CFD methods can be utilized for a variety of applications including steady and unsteady flow predictions around ship hulls and superstructures. The result may include resistance, propulsion as well as sea

keeping properties and contains forces and moments acting on the ship. It also provides insight into the flow field around it. Depending on the objective, different levels of physical simplifications can be made. The potential flow methods are the most popular ones due to their short computation time. However, these methods disregard viscous effects and are used mainly for wave resistance prediction and minimization Jensen (1989), Raven (1992), Janson (1997). More elaborate methods solve the Reynolds Averaged Navier-Stokes (RANS) equations with turbulence modelling. With these methods, the entire flow field around ship hulls, appendages, and propulsors as well as superstructures can be simulated.

In order to simulate free surface flows with gravity waves, the RANS methods use surface tracking or surface capturing techniques. Additional equations are solved, providing information about the interface location. The position may be followed by an adaptive grid, such as in surface tracking methods or captured within a fixed grid, as in surface capturing methods. The first one gives sharp boundaries between water and air, but the grid adaptation to complex geometries of breaking waves can be difficult. The latter is more flexible, and large deformations of the interface, air entrapment, wave breaking, and spray can be handled. However, this requires sophisticated numerical approaches to keep the interface sharp and stable at the same time.

For many years research within computational fluid dynamics (CFD) was focused on higher order and anti-diffusive discretization schemes. Very good results can be achieved with regard to accuracy and sharpness of the interface but often stability is compromised and therefore methods are difficult to apply on more general cases. Recently, grid refinements are becoming increasingly popular Hay, (2005). The grid resolution is increased only in the areas that require better spatial representation. There are two basic approaches that can be recognized. Either an unstructured single grid is subdivided into more cells locally or more than one grid is used to form overlapping grids, also known as overset grids. There are several groups working on overlapping grid techniques around the world. The most well-known RANS general code with overlapping technique is Overture, Henshaw (1994). In naval applications the leading codes that incorporate this solution are SHIPFLOW from FLOWTECH International AB and CFDSHIP-IOWA, from University of Iowa. The latter successfully uses overlapping grid refinements of the free surface vicinity, while the first one so far has had no free surface capability. The overlapping grids have been used to refine or represent complex geometries and appendages, Regnström (2000).

1.3 Present Contributions

In this work, the SHIPFLOW steady state RANS code is extended to include the computation of free surface flows. A volume-of-fluid (VOF) surface capturing method is used to locate the water-air interface and the overlapping grid is complemented with an adaptive free surface interface refinement.

Various discretization schemes for convective fluxes, with an emphasis on the water fraction transport equation have been investigated. This particular equation requires a special attention in order to keep the air and water interface as sharp

as possible, at the same time avoiding non-physical solutions. Several schemes were implemented and tested in order to find a suitable method.

The second interesting feature of the implementation is that the free-surface solution is computed with an artificial time step as opposed to other well established codes which use time dependent techniques to acquire the steady state wave height.

Finally, the overlapping grid technique is applied to refine the spatial resolution near the free-surface. An attempt to adapt the refinement grid to the wave profile is made.

1.4 Structure of the thesis

The thesis is divided in six chapters. The major parts deal with mathematical and numerical modelling, the overlapping adaptive grid technique and validation of the methods applied. In the final chapter the work is summarised and suggestions for the future are given.

2 MATHEMATICAL MODEL

2.1 Introduction

The continuity, momentum and energy equations are the fundamental governing equations of fluid dynamics. In the CFD literature the system of those equations is commonly named the Navier-Stokes equations and a brief introduction will be given in subsequent sections. A formulation suitable for viscous free surface simulations is highlighted and a surface capturing technique presented.

2.2 Flow equations

The fluid motion, also in aero- and hydro-dynamics of ships, can be described by the Navier-Stokes equations obtained by applying Newton's second law to a fluid element and assuming that the viscous stress is proportional to the strain rate. However, the Navier-Stokes equations cannot be solved for cases of practical interest because they contain too small scales to resolve. Therefore, the equations are time averaged, Larsson and Raven (2010), to remove turbulence scales from the simulations at the expense of introducing the new unknowns, known as Reynolds stresses. The time averaged equations are called Reynolds-averaged Navier-Stokes, RANS, equations. Separate equations are required for Reynolds stresses. In the continuous model the fluid is modelled as a mixture of air and water so the same equations can be used to model both. Considering the fact that the gravity is the only body force acting on the particle and is directed along the z , axis vertically upwards, the steady state, incompressible RANS equations in a component form will be:

$$\begin{aligned} \frac{\partial}{\partial x}(\rho u^2 + p) + \frac{\partial}{\partial y}(\rho uv) + \frac{\partial}{\partial z}(\rho uw) &= (\frac{\partial \tau_{xx}}{\partial x} + \frac{\partial \tau_{xy}}{\partial y} + \frac{\partial \tau_{xz}}{\partial z}) \\ \frac{\partial}{\partial x}(\rho uv) + \frac{\partial}{\partial y}(\rho v^2 + p) + \frac{\partial}{\partial z}(\rho vw) &= (\frac{\partial \tau_{yx}}{\partial x} + \frac{\partial \tau_{yy}}{\partial y} + \frac{\partial \tau_{yz}}{\partial z}) \\ \frac{\partial}{\partial x}(\rho uw) + \frac{\partial}{\partial y}(\rho vw) + \frac{\partial}{\partial z}(\rho w^2 + p) &= (\frac{\partial \tau_{zx}}{\partial x} + \frac{\partial \tau_{zy}}{\partial y} + \frac{\partial \tau_{zz}}{\partial z}) - \rho g \end{aligned} \quad (1)$$

where u , v , w are the mean velocity components, p is the mean pressure plus $\frac{2}{3}\rho k$, ρ is the density and g is the acceleration of gravity. The stress tensor τ_{ij} is defined as:

$$\tau_{ij} = (\mu + \mu_T)(\frac{\partial u_i}{\partial x_j} + \frac{\partial u_j}{\partial x_i}), \quad (2)$$

where μ is the dynamic viscosity and μ_T the turbulent dynamic viscosity used to model the Reynolds stresses according to Boussinesq approximation, Larsson and Raven (2010). k is the turbulent kinetic energy.

The flow is solved both in air and water. The ρ and μ are discontinuous at the interface with pure air above it and pure water below.

The RANS equations are solved together with the continuity equation, that describes the conservative transport of mass, is derived. It is based on the fact that the total net mass transport out of the control volume must be zero when no sources are included. For incompressible fluids the equation is as follows:

$$\frac{\partial u}{\partial x} + \frac{\partial v}{\partial y} + \frac{\partial w}{\partial z} = 0 \quad . \quad (3)$$

2.3 Interface capturing method

The formulations (1) and (3) allow for a variable density, which is used here to represent a mixture of two incompressible fluids in a continuous manner. In addition to the described mass and momentum conservation equations, a water fraction α , transport equation is introduced which is derived from the mass conservation equation for the water only.

$$\frac{\partial}{\partial x}(\alpha u) + \frac{\partial}{\partial y}(\alpha v) + \frac{\partial}{\partial z}(\alpha w) = 0 \quad , \quad (4)$$

where α indicates the amount of water in the mixture and takes values from 0 to 1. The density and dynamic viscosity for pure fluids are considered constant – incompressible flow – however the mixture used in equations (1) varies in the domain. Therefore the density and the dynamic viscosity at each location are proportional to the water fraction α :

$$\begin{aligned} \mu &= \alpha \mu_w + (1 - \alpha) \mu_a \quad , \\ \rho &= \alpha \rho_w + (1 - \alpha) \rho_a \quad . \end{aligned} \quad (5)$$

2.4 Turbulence model

The Menter $k-\omega$ SST turbulence model, Menter (1993), is used in the current implementation to compute u_T . The model is valid all the way to the solid walls, so there is no need for wall functions. No special treatment is applied near the free surface interface. The $k-\omega$ SST combines good properties of the $k-\omega$ model near the wall and $k-\epsilon$ outside of this region using blending or switching functions. Since the main focus of this paper is to provide information on the free surface modelling in the code no further details on the turbulence model will be given. More details can be found in Broberg et al. (2007).

2.5 Boundary conditions

To solve the system of equations appropriate boundary conditions (BC) are necessary. Two basic boundary conditions are used: Dirichlet and Neumann. The first specifies the value of a solution at the domain boundaries and the latter

specifies values of the derivative normal to the surface of a solution. These are used then according to the physical properties of different types of boundaries that define a computational problem, Versteg and Malalasekra (1995).

Inlet. At the inlet it is assumed that the flow is undisturbed. Constant values are prescribed for the velocity as well as the turbulent quantities. The void fraction is also described with the Dirichlet BC, but the fraction varies at the inlet face. It gets values equal to 1 in the water and 0 in the air. The pressure gradient in the longitudinal direction is set to zero.

Outlet. A simplification is made that the boundary is far downstream, which means that the flow is fully developed and that the waves are entirely damped. Therefore, it is acceptable to use the Neumann BC for the velocity, void fraction and turbulent quantities. For the current surface capturing method implementation the Neumann BC is also used for the pressure.

Slip. The physical boundaries-such as top, bottom and side faces of the domain are assumed solid walls and create an enclosed space in which the hull is placed. No flow through such a boundary is ensured – the normal velocity component is zero – and the flow is free to slip along the boundaries – the normal velocity gradient is zero. The Neumann BC is used for the pressure, void fraction and turbulent quantities. The same conditions are used at the symmetry plane. The slip condition is a good approximation for the symmetry plane and also the outer boundary if the computational domain is large compared to the ship dimensions. A modified slip condition is applied to a part of the top boundary. The Dirichlet BC is used for the pressure in order to solve the equations.

Noslip. At the hull surface the velocity is zero i.e. no flow through the boundary is possible and the fluid sticks to the surface. The Neumann BC is used for the pressure and void fraction.

3 NUMERICAL METHOD

The partial differential equations are discretized to algebraic equations with the Finite Volume Method (FVM). The averaged values in each cell volume surrounding the centres are calculated from face fluxes. The flux entering a volume through a face equals the flux leaving the adjacent volume through that face and therefore the method is conservative.

3.1 Governing equations in vector form

The system of equations (1) and (3) in conservation form including the turbulence equations can be represented in a generic, vector form by

$$\frac{\partial \mathbf{f}}{\partial x} + \frac{\partial \mathbf{g}}{\partial y} + \frac{\partial \mathbf{h}}{\partial z} = \frac{\partial \mathbf{f}_v}{\partial x} + \frac{\partial \mathbf{g}_v}{\partial y} + \frac{\partial \mathbf{h}_v}{\partial z} + \mathbf{r} \quad (6)$$

where \mathbf{f} , \mathbf{g} , \mathbf{h} , \mathbf{f}_v , \mathbf{g}_v , \mathbf{h}_v , \mathbf{r} are column vectors. The column vectors on the left side of the equation (6), given by \mathbf{f} , \mathbf{g} , and \mathbf{h} represent inviscid fluxes, while \mathbf{f}_v , \mathbf{g}_v , and \mathbf{h}_v represent viscous fluxes.

$$\mathbf{f} = \begin{vmatrix} u^2 \rho + p \\ uv \rho \\ uw \rho \\ u \alpha \\ uk \\ u \omega \end{vmatrix}, \quad \mathbf{g} = \begin{vmatrix} uv \rho \\ v^2 \rho + p \\ vw \rho \\ v \alpha \\ vk \\ v \omega \end{vmatrix}, \quad \mathbf{h} = \begin{vmatrix} wu \rho \\ wv \rho \\ w^2 \rho + p \\ w \alpha \\ wk \\ w \omega \end{vmatrix} \quad (7)$$

$$\mathbf{f}_v = \begin{vmatrix} \tau_{xx} \\ \tau_{yx} \\ \tau_{zx} \\ 0 \\ 0 \\ v_k \frac{\partial k}{\partial x} \\ v_\omega \frac{\partial \omega}{\partial x} \end{vmatrix}, \quad \mathbf{g}_v = \begin{vmatrix} \tau_{xy} \\ \tau_{yy} \\ \tau_{zy} \\ 0 \\ 0 \\ v_k \frac{\partial k}{\partial y} \\ v_\omega \frac{\partial \omega}{\partial y} \end{vmatrix}, \quad \mathbf{h}_v = \begin{vmatrix} \tau_{xz} \\ \tau_{yz} \\ \tau_{zz} \\ 0 \\ 0 \\ v_k \frac{\partial k}{\partial z} \\ v_\omega \frac{\partial \omega}{\partial z} \end{vmatrix} \quad (8)$$

$$\mathbf{r} = \begin{pmatrix} 0 \\ 0 \\ -g \\ 0 \\ 0 \\ 0 \\ 0 \end{pmatrix} \quad (9)$$

The flux vectors of the equations (1), (3) and (4) are split into convective (7) and viscous (8) fluxes. The right side, vector \mathbf{r} , represents the source term, which in our case is the gravity force acting in the z-axis direction (9).

3.2 Discretization

In the FVM the variation of flow properties is approximated between cells with differencing schemes. An appropriate scheme is chosen to support the physical behaviour of the flow in the best possible manner. The diffusion terms are discretized with central differences while for convection hybrid schemes are used.

3.2.1 Convection term

The convective fluxes discretization is based on the first order Roe type flux difference splitting algorithm, Roe (1981). Higher order accuracy is achieved by an explicit defect correction with flux extrapolation presented by Dick and Linden (1992) and extended with several types of limiters in order to find suitable solutions for different equations.

3.2.2 Roe fluxes

The convective flux differences can be written:

$$\Delta \mathbf{f} = \overline{A}_1(\Delta \mathbf{q}) \quad , \quad \Delta \mathbf{g} = \overline{A}_2(\Delta \mathbf{q}) \quad , \quad \Delta \mathbf{h} = \overline{A}_3(\Delta \mathbf{q}) \quad (10)$$

where $\mathbf{q} = (u, v, w, p, \alpha, k, w)^T$ and the discrete Jacobians are:

$$A_1 = \begin{pmatrix} 2\rho u & 0 & 0 & 1 & 0 & 0 & 0 \\ \rho v & \rho u & 0 & 0 & 0 & 0 & 0 \\ \rho w & 0 & \rho u & 0 & 0 & 0 & 0 \\ 1 & 0 & 0 & 0 & 0 & 0 & 0 \\ \alpha & 0 & 0 & 0 & u & 0 & 0 \\ k & 0 & 0 & 0 & 0 & u & 0 \\ \omega & 0 & 0 & 0 & 0 & 0 & u \end{pmatrix}, \quad A_2 = \begin{pmatrix} \rho v & \rho u & 0 & 0 & 0 & 0 & 0 \\ 0 & 2\rho v & 0 & 1 & 0 & 0 & 0 \\ 0 & \rho w & \rho v & 0 & 0 & 0 & 0 \\ 0 & 1 & 0 & 0 & 0 & 0 & 0 \\ 0 & \alpha & 0 & 0 & v & 0 & 0 \\ 0 & k & 0 & 0 & 0 & v & 0 \\ 0 & \omega & 0 & 0 & 0 & 0 & v \end{pmatrix}, \quad (11)$$

$$A_3 = \begin{pmatrix} \rho w & 0 & \rho u & 0 & 0 & 0 & 0 \\ 0 & \rho w & \rho v & 0 & 0 & 0 & 0 \\ 0 & 0 & 2\rho w & 1 & 0 & 0 & 0 \\ 0 & 0 & 1 & 0 & 0 & 0 & 0 \\ 0 & 0 & \alpha & 0 & w & 0 & 0 \\ 0 & 0 & k & 0 & 0 & w & 0 \\ 0 & 0 & \omega & 0 & 0 & 0 & w \end{pmatrix}$$

The eigensystem is evaluated for a linear combination of the Jacobians $A = n_x A_1 + n_y A_2 + n_z A_3$, with dependent variables calculated at the interface between the two states.

3.2.3 Eigensystem

The eigenvalues (12), left and right eigenvectors (13) of the matrix A are

$$\lambda_{1,2,3,4,5,6,7} = b, b, b, b, b, -a+b, a+b, \quad , \quad (12)$$

$$R = \begin{pmatrix} 0 & 0 & 0 & -n_z & -n_y & \frac{-\beta^2 n_x + au - bu}{a\beta^2 \rho} & \frac{\beta^2 n_x + au + bu}{a\beta^2 \rho} \\ 0 & 0 & 0 & -n_z & n_x + n_z & \frac{-\beta^2 n_y + av - bv}{a\beta^2 \rho} & \frac{\beta^2 n_y + av + bv}{a\beta^2 \rho} \\ 0 & 0 & 0 & n_x + n_y & -n_y & \frac{-\beta^2 n_z + aw - bw}{a\beta^2 \rho} & \frac{\beta^2 n_z + aw + bw}{a\beta^2 \rho} \\ 0 & 0 & 0 & 0 & 0 & 1 & 1 \\ 0 & 0 & 1 & 0 & 0 & 0 & 0 \\ 0 & 1 & 0 & 0 & 0 & 0 & 0 \\ 1 & 0 & 0 & 0 & 0 & 0 & 0 \end{pmatrix} \quad (13)$$

and

$$L = R^{-1},$$

where for clarity and simplification $b = n_x u + n_y v + n_z w$, $n_x^2 + n_y^2 + n_z^2 = 1$ and $a = \sqrt{\beta^2 + b^2}$.

The matrix A is rewritten by using eigendecomposition and split into positive and negative parts

$$A = A^+ + A^- \quad (14)$$

with

$$A^+ = R\Lambda^+ L \quad , \quad A^- = R\Lambda^- L \quad , \quad (15)$$

where the positive and negative diagonal eigenvalue matrices are formed by

$$\Lambda^+ = \text{diag}(\lambda_1^+, \lambda_2^+, \lambda_3^+, \lambda_4^+, \lambda_5^+, \lambda_6^+, \lambda_7^+) \quad , \quad \Lambda^- = \text{diag}(\lambda_1^-, \lambda_2^-, \lambda_3^-, \lambda_4^-, \lambda_5^-, \lambda_6^-, \lambda_7^-) \quad (16)$$

created by applying min – max functions to the original eigenvalues:

$$\lambda_i^+ = \max(\lambda_i, 0) \quad , \quad \lambda_i^- = \min(\lambda_i, 0) \quad .$$

The splitting of the combined Jacobian matrices (15) as described above makes it also possible to split any linear combinations of flux differences which constitutes a basis for the discretization used in the code. The flux difference then can be written

$$\Delta\phi \equiv n_x \Delta f + n_y \Delta g + n_z \Delta h = A^+ \Delta q + A^- \Delta q \quad . \quad (17)$$

3.2.4 First order upwind formulation

We will consider the inviscid part of equation (6) in a 2D control volume as shown in Figure 2.

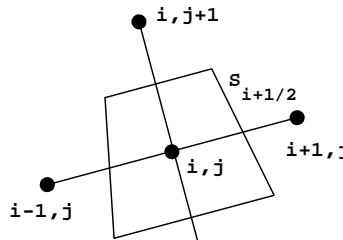


Figure 2: Control volume.

The upwind definition of the flux at face $i+\frac{1}{2}$ is

$$F_{i+\frac{1}{2}} = \frac{1}{2}(F_i + F_{i+1}) - \frac{1}{2}|\Delta F_{i,i+1}| \quad (18)$$

and flux difference over the surface $S_{i+\frac{1}{2}}$ is:

$$\Delta F_{i,i+1} = F_{i+1} - F_i = \Delta s_{i+\frac{1}{2}}(n_x \Delta f_{i,i+1} + n_y \Delta g_{i,i+1}) = \Delta s_{i+\frac{1}{2}} A_{i,i+1} \Delta \xi_{i,i+1} \quad (19)$$

where $\Delta \xi^T = (u, v, p, \alpha, k, \omega)$ is the vector of dependent variables.

The Jacobian matrices are further split into positive and negative parts and the absolute value of the flux difference can be written as:

$$|\Delta F_{i,i+1}| = \Delta s_{i+\frac{1}{2}} (A_{i,i+1}^+ - A_{i,i+1}^-) \Delta \xi_{i,i+1} \quad (20)$$

The inviscid flux balance over the control volume is:

$$F_{i+\frac{1}{2}} - F_{i-\frac{1}{2}} + F_{j+\frac{1}{2}} - F_{j-\frac{1}{2}} = 0 \quad , \quad (21)$$

the first term can be rewritten to:

$$\begin{aligned} F_{i+\frac{1}{2}} &= \frac{1}{2}(F_i + F_{i+1}) - \frac{1}{2}|\Delta F_{i,i+1}| = \frac{1}{2}(F_i + F_i + \Delta F_{i,i+1}) - \frac{1}{2}|\Delta F_{i,i+1}| = \\ &= F_i + \frac{1}{2}\Delta F_{i,i+1} - \frac{1}{2}|\Delta F_{i,i+1}| = \\ F_i &+ \frac{1}{2}\Delta s_{i+\frac{1}{2}} (A_{i,i+1}^+ + A_{i,i+1}^-) \Delta \xi_{i,i+1} - \frac{1}{2}\Delta s_{i+\frac{1}{2}} (A_{i,i+1}^+ - A_{i,i+1}^-) \Delta \xi_{i,i+1} = \\ &= F_i + \Delta s_{i+\frac{1}{2}} A_{i,i+1}^- \Delta \xi_{i,i+1} \end{aligned} \quad (22)$$

and the second to:

$$\begin{aligned} F_{i-\frac{1}{2}} &= \frac{1}{2}(F_i + F_{i-1}) - \frac{1}{2}|\Delta F_{i-1,i}| = \frac{1}{2}(F_i + F_i + \Delta F_{i-1,i}) - \frac{1}{2}|\Delta F_{i-1,i}| = \\ &= F_i + \frac{1}{2}\Delta F_{i-1,i} - \frac{1}{2}|\Delta F_{i-1,i}| = \\ F_i &- \frac{1}{2}\Delta s_{i-\frac{1}{2}} (A_{i-1,i}^+ + A_{i-1,i}^-) \Delta \xi_{i-1,i} - \frac{1}{2}\Delta s_{i-\frac{1}{2}} (A_{i-1,i}^+ - A_{i-1,i}^-) \Delta \xi_{i-1,i} = \\ &= F_i - \Delta s_{i-\frac{1}{2}} A_{i-1,i}^+ \Delta \xi_{i-1,i} \end{aligned} \quad (23)$$

Hence the resulting flux balance is:

$$\begin{aligned} F_i + \Delta s_{i+\frac{1}{2}} A_{i,i+1}^- \Delta \xi_{i,i+1} - F_i - \Delta s_{i-\frac{1}{2}} A_{i-1,i}^+ \Delta \xi_{i-1,i} + F_j + \\ F_j + \Delta s_{j+\frac{1}{2}} A_{j,j+1}^- \Delta \xi_{j,j+1} - F_j - \Delta s_{j-\frac{1}{2}} A_{j-1,j}^+ \Delta \xi_{j-1,j} = \\ \Delta s_{i+\frac{1}{2}} A_{i,i+1}^- \Delta \xi_{i,i+1} + \Delta s_{i-\frac{1}{2}} A_{i-1,i}^+ \Delta \xi_{i-1,i} + \Delta s_{j+\frac{1}{2}} A_{j,j+1}^- \Delta \xi_{j,j+1} + \Delta s_{j-\frac{1}{2}} A_{j-1,j}^+ \Delta \xi_{j-1,j} = 0 \end{aligned} \quad (24)$$

3.2.5 Second order formulation

The second order accuracy is obtained with the explicit correction defined in Dick and Linden (1992) which stems from the Chakravarthy and Osher (1985) formulation. In the latter formulation the second order correction is defined by shifted eigenvalues together with the geometric terms of the face, while in the

first formulation the problem is simplified by leaving the eigenvalues calculated for the central face assuming that, in practice, the difference is small. In the correction to second order, additional terms are introduced and the flux is composed of limited upwind and central fluxes.

A pure second order upwind flux is as follows:

$$F_{i+\frac{1}{2}} = \frac{1}{2}(F_i + F_{i+1}) - \frac{1}{2} \sum_n \Delta F_{i,i+1}^{n+} + \frac{1}{2} \sum_n \Delta F_{i,i+1}^{n-} + \frac{1}{2} \sum_n \widetilde{\Delta F}_{i-1,i}^{n+} - \frac{1}{2} \sum_n \widetilde{\Delta F}_{i+1,i}^{n-}. \quad (25)$$

where $\widetilde{\Delta F}_{i-1,i}^{n+} = \Delta s_{i+\frac{1}{2}} r_{i+\frac{1}{2}}^n \lambda_{i+\frac{1}{2}}^n l_{i+\frac{1}{2}}^n \Delta \xi_{i-\frac{1}{2}}$ and

a pure second order central difference flux is:

$$\bar{F}_{i+\frac{1}{2}} = \frac{1}{2}(F_i + F_{i+1}) \quad (26)$$

To obtain results with a low numerical diffusion but maintaining stability a high resolution scheme is constructed based on a hybrid of upwind and central differences flux with help of limiters:

$$F_{i+\frac{1}{2}} = \frac{1}{2}(F_i + F_{i+1}) - \frac{1}{2} \sum_n \Delta F_{i,i+1}^{n+} + \frac{1}{2} \sum_n \Delta F_{i,i+1}^{n-} + \frac{1}{2} \sum_n \widetilde{\Delta F}_{i-1,i}^{n+} - \frac{1}{2} \sum_n \widetilde{\Delta F}_{i+1,i}^{n-}. \quad (27)$$

where the limited values are

$$\widetilde{\Delta F}_{i+1,i+2}^{n-} = \lim(\widetilde{\Delta F}_{i+1,i+2}^{n-}, \Delta F_{i,i+1}^{n-}) \quad (28)$$

and \lim denotes a limited combination of both arguments.

3.3 Flux limiters

The flux limiters are incorporated into the discretization scheme in order to avoid wiggles in the solution that may occur due to not monotonicity-preserving schemes such as central or fully upwind. The limiter functions, denoted in the previous section as \lim , select an appropriate argument based on their mutual relations which can indicate non-physical oscillations, overshoots to non-realistic values of the solution. Stable results are achieved with blending of schemes and locally lowering the order of accuracy. The most well-known techniques for constructing and analysing the schemes are those by Sweby (1984) and Leonard (1991). In this report the latter one is used.

3.3.1 Normalised Variable Diagram

The higher resolution schemes can be constructed based on a Normalised Variable Diagram (NVD) which are described in detail by Leonard (1991). This

approach helps to determine the face value from surrounding cell centres.

In Figure 3 a one-dimensional control volume is illustrated and the face value on the left side of that volume is considered. The cell centres that are used for the face value reconstruction are depicted as D, C and U and their order depends on the flow direction at the face. This abbreviation comes from their relative location and indicates the downstream, central and upstream cells. It should be noted that in case of the current implementation the recognition of the flow direction is taken care of by the underlying Roe discretization scheme that is inherently upwind.

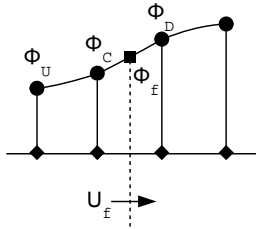


Figure 3: Definition of upstream (U), central (C) and downstream (D) nodes with respect to flow direction.

Any value ϕ in the shown group of cells can be normalized with respect to the difference between the downstream and upstream values:

$$\tilde{\phi} = \frac{\phi - \phi_U}{\phi_D - \phi_U} . \quad (29)$$

Applying this normalization to the cell centre values surrounding the face, Figure 4, it can be seen that the normalized face value depends only on the normalized centre cell since the other normalized node values are constant: $\tilde{\phi}_U = 0$ and $\tilde{\phi}_D = 1$.

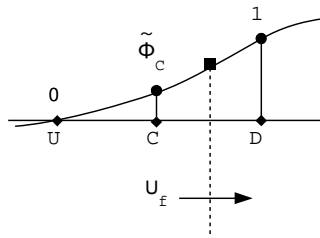


Figure 4: Normalized node values.

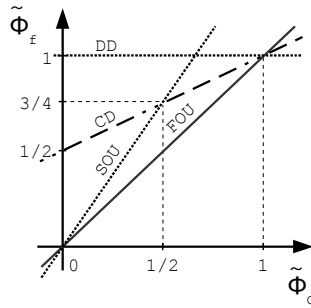


Figure 5: NVD for basic differencing schemes.

The scheme constructed using NVD diagram can be used thereafter to find a real face value by using the normalised face value:

$$\phi_f = \phi_c - (\phi_c - \phi_U) + \tilde{\phi}_f [(\phi_D - \phi_c) + (\phi_c - \phi_U)] . \quad (30)$$

The $\tilde{\phi}_f$ is then chosen in such a way that the desired scheme is created. The basic schemes are plotted in the NVD, Figure 5, and have the following normalized face values:

Abbreviation	Scheme type	Normalised face value
FOU	first order upwind	$\tilde{\phi}_f = \tilde{\phi}_c$
SOU	second order upwind	$\tilde{\phi}_f = \frac{3}{2} \tilde{\phi}_c$
CD	central	$\tilde{\phi}_f = \frac{1}{2}(1 + \tilde{\phi}_c)$
DD	downwind	$\tilde{\phi}_f = 1$

It is however virtually impossible to use the above schemes for convective terms in their pure form. The perfect scheme needs to be accurate to avoid excessive numerical diffusion, stable and bounded to physical values. However no scheme possesses these qualities simultaneously. High resolution composite schemes have been developed to overcome problems with non-physical oscillations and overshoots of a solution. A Convective Boundedness Criterion, CBC, proposed by Gaskell and Lau (1998), and more restrictive constraint called Total Variation Diminishing, TVD, introduced by Harten (1983) help to maximize accuracy while at the same time preserving the stability and boundedness. Both criteria are illustrated in the NVD diagrams in Figure 6.

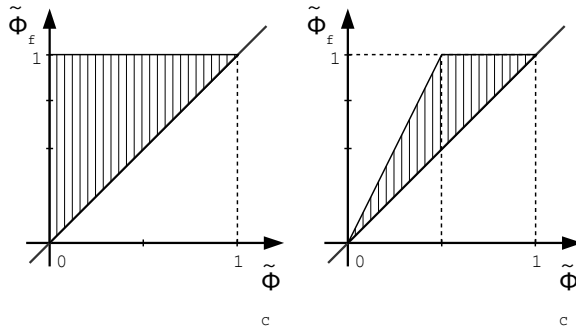


Figure 6: CBC and TVD criteria.

3.3.2 Common schemes for convection

In the present method the base for the momentum and continuity equations is the MUSCL scheme. Additionally several schemes have been tested for the water fraction transport equation. In order to keep the air and water interface sharp a certain amount of anti-diffusion is required. A scheme that can sharpen the step discontinuity of the fluid density should be used. Therefore, the transport equation for the volume fraction usually uses a special scheme that possesses this feature. Here, several linear and non-linear schemes were investigated, including the more diffusive ones, Osher and MUSCL and the compressive schemes SuperBee, Super-C and SuperBee-C. For references, see Figures 7a through 7h. Another family, the so called blended schemes, is represented here by STACS, Darwish and Moukalled (2006). This scheme blends diffusive and highly compressive schemes depending on the angle between the free surface interface and the control volume face.

The Osher method, Chakravarthy and Osher (1985), Figure 7b, is related to the basic Minimum Modulus, MinMod, of Roe, Figure 7a. It uses second-order upwinding combined with first-order downwinding instead of central differences which makes it less diffusive. The difference is substantial between these two schemes and makes the Osher scheme an acceptable solution for convection equations that do not need to resolve extremely steep gradients such as the water fraction variation at the interface.

The MUSCLE scheme by Van Leer (1979), Figure 7c, is based on the Fromm method, Fromm (1968) in the region near $\tilde{\phi}_c=0.5$. It is, however, altered with piecewise modifications passing through $(0,0)$ and $(1,1)$ in the NVD, using a monotonic limiter in the lower range and first order downwinding in the upper. The first-order upwind method is used elsewhere. The scheme performs better than Osher, however still it is not a suitable solution for water fraction transport equation.

A scheme called SuperBee developed by Roe (1985), Figure 7d, is one of the most compressive schemes. The normalized face value is a piecewise linear function constructed with slopes of $2\tilde{\phi}_c$ in the lower part, central differences and second-order upwind near $\tilde{\phi}_c=0.5$, and first-order downwind in the upper

part of the NVD. It is able to represent step changes in the computed flow quantities which makes it very suitable for free surface applications.

The next more extreme scheme is the Super-C, Leonard (1988), Figure 7e. The name suggests that the scheme is "super compressive" and indeed the step changes are represented with steeper gradients than in case of SuperBee. The piecewise linear function in the NVD follows the contour of central differences, second-order upwind and first-order downwind. The most compressive scheme is Hyper-C, Figure 7g. It is using limited first-order downwinding.

The tests run with the Super-C and Hyper-C methods indicated some stability issues. Also their requirement to keep the Courant number low increased the computation time. An idea of a scheme that would be somewhere between the SuperBee and Super-C arose, Figure 7f. A parameter to control the lower part of the NVD was introduced in such a way that the amount of central differencing could be adjusted. A natural way of naming the scheme seemed to be SuperBee-C. The parameter was thereafter adjusted based on test calculations and a good compromise turned out to be closer to the Super-C scheme with the central differencing clipped in the lower part of the NVD with a line sloping at around $16\tilde{\phi}_c$.

As a reference the Switching Techniques for Advection and Capturing of Surfaces (STACS) scheme was implemented, Figure 7h, which was found to outperform well established HRIC and CICSAM, Darwish and Moukalled (2006). This blended scheme is switching, as stated in Darwish, between the STOIC, high resolution scheme and the SuperBee, compressive scheme, which however seems to be defined differently than the one in Leonard (1998). The blending depends on the angle between the normal to the interface and the normal to the cell face. When the interface is parallel to the face the compressive scheme is used. The blending function $[\cos(\Theta)]^4$ allows for rapid changes away from the compressive to the high-resolution scheme when the interface is not along the grid direction.

Results of the calculations with various schemes are presented in Chapter 5.

Scheme	Definition with Normalised Variable	Normalised Variable Diagram
a. MinMod, (Roe 1986)	$\tilde{\phi}_f = \begin{cases} \frac{3}{2}\tilde{\phi}_c & \text{for } 0 \leq \tilde{\phi}_c \leq \frac{1}{2} \\ \frac{1}{2}(1+\tilde{\phi}_c) & \frac{1}{2} \leq \tilde{\phi}_c \leq 1 \\ \tilde{\phi}_c & \text{otherwise} \end{cases}$	<p>The diagram shows the relationship between the normalised flux $\tilde{\phi}_f$ on the vertical axis and the normalised variable $\tilde{\phi}_c$ on the horizontal axis. Both axes range from 0 to 1, with major ticks at 0, 1/2, and 1. A diagonal line represents the identity function $\tilde{\phi}_f = \tilde{\phi}_c$. Two other curves are plotted: the SOD curve (Solid Oblique Down) and the Fromm curve. The SOD curve is concave down, starting at (0,0), passing through (1/2, 1/2), and ending at (1, 1). The Fromm curve is concave up, starting at (0,0), passing through (1/2, 1/2), and ending at (1, 1). Dashed lines indicate the mapping for a given $\tilde{\phi}_c$ value.</p>
b. Osher, (Chakravarthy and Osher 1983)	$\tilde{\phi}_f = \begin{cases} \frac{3}{2}\tilde{\phi}_c & \text{for } 0 \leq \tilde{\phi}_c \leq \frac{2}{3} \\ 1 & \frac{2}{3} \leq \tilde{\phi}_c \leq 1 \\ \tilde{\phi}_c & \text{otherwise} \end{cases}$	<p>The diagram is similar to the one above, showing the relationship between $\tilde{\phi}_f$ and $\tilde{\phi}_c$. The axes range from 0 to 1. The identity line, SOD curve, and Fromm curve are present. The SOD curve starts at (0,0), passes through (2/3, 1), and ends at (1, 1). The Fromm curve starts at (0,0), passes through (2/3, 1), and ends at (1, 1).</p>
c. MUSCL, (Van Leer 1979)	$\tilde{\phi}_f = \begin{cases} 2\tilde{\phi}_c & \text{for } 0 < \tilde{\phi}_c < \frac{1}{4} \\ \frac{1}{4} + \tilde{\phi}_c & \frac{1}{4} \leq \tilde{\phi}_c \leq \frac{3}{4} \\ 1 & \frac{3}{4} \leq \tilde{\phi}_c \leq 1 \\ \tilde{\phi}_c & \text{otherwise} \end{cases}$	<p>The diagram shows the relationship between $\tilde{\phi}_f$ and $\tilde{\phi}_c$. The axes range from 0 to 1. The identity line, SOD curve, and Fromm curve are present. The SOD curve starts at (0,0), passes through (1/4, 1/4), (3/4, 3/4), and (1, 1). The Fromm curve starts at (0,0), passes through (1/4, 1/4), (3/4, 3/4), and (1, 1).</p>
d. SuperBee, (Roe 1985)	$\tilde{\phi}_f = \begin{cases} 2\tilde{\phi}_c & \text{for } 0 < \tilde{\phi}_c < \frac{1}{3} \\ \frac{1}{2}(1+\tilde{\phi}_c) & \frac{1}{3} \leq \tilde{\phi}_c < \frac{1}{2} \\ \frac{3}{2}\tilde{\phi}_c & \frac{1}{2} \leq \tilde{\phi}_c < \frac{2}{3} \\ 1 & \frac{2}{3} \leq \tilde{\phi}_c < 1 \\ \tilde{\phi}_c & \text{otherwise} \end{cases}$	<p>The diagram shows the relationship between $\tilde{\phi}_f$ and $\tilde{\phi}_c$. The axes range from 0 to 1. The identity line, SOD curve, and Fromm curve are present. The SOD curve starts at (0,0), passes through (1/3, 1/3), (2/3, 2/3), and (1, 1). The Fromm curve starts at (0,0), passes through (1/3, 1/3), (2/3, 2/3), and (1, 1).</p>

<p>e. Super-C, (Leonard 1988)</p>	$\tilde{\phi}_f = \begin{cases} \frac{1}{2}(1+\tilde{\phi}_c) & \text{for } 0 < \tilde{\phi}_c < \frac{1}{2} \\ \frac{3}{2}\tilde{\phi}_c & \frac{1}{2} \leq \tilde{\phi}_c < \frac{2}{3} \\ 1 & \frac{2}{3} \leq \tilde{\phi}_c < 1 \\ \tilde{\phi}_c & \text{otherwise} \end{cases}$	
<p>f. SuperBee-C</p>	$\tilde{\phi}_f = \begin{cases} k\tilde{\phi}_c & \text{for } 0 < \tilde{\phi}_c < \frac{1}{2k-1} \\ \frac{1}{2}(1+\tilde{\phi}_c) & \frac{1}{2k-1} \leq \tilde{\phi}_c < \frac{1}{2} \\ \frac{3}{2}\tilde{\phi}_c & \frac{1}{2} \leq \tilde{\phi}_c < \frac{2}{3} \\ 1 & \frac{2}{3} \leq \tilde{\phi}_c < 1 \\ \tilde{\phi}_c & \text{otherwise} \end{cases}$ <p>where $k > 2$ becomes: SuperBee for $k=2$ and Super-C for $k=\infty$</p>	
<p>g. HyperC, (Leonard 1988)</p>	$\tilde{\phi}_f = \begin{cases} \min(1, \frac{\tilde{\phi}_c}{Co}) & \text{for } 0 \leq \tilde{\phi}_c \leq 1 \\ \tilde{\phi}_c & \text{otherwise} \end{cases}$	
<p>h. STACS, (Darwish 2006)</p>	$\tilde{\phi}_{f, STACS} = \tilde{\phi}_{f, SuperBee} [\cos(\Theta)]^4 + \tilde{\phi}_{f, STOIC} (1 - [\cos(\Theta)]^4)$ <p>where Θ is the angle between the gradient of the volume fraction at the interface and the normal to the cell face</p> <p>and</p> $\tilde{\phi}_{f, STOIC} = \begin{cases} \frac{1}{2}(1+\tilde{\phi}_c) & 0 \leq \tilde{\phi}_c < \frac{1}{2} \\ \frac{3}{8} + \frac{3}{4}\tilde{\phi}_c & \frac{1}{2} \leq \tilde{\phi}_c < \frac{5}{6} \\ 1 & \frac{5}{6} \leq \tilde{\phi}_c < 1 \\ \tilde{\phi}_c & \text{otherwise} \end{cases}$	

Figure 7: NVD diagrams.

3.4 Diffusion terms

The diffusion terms of the turbulent incompressible Navier-Stokes equations (6) are:

$$\begin{aligned}
 \frac{\partial}{\partial x_j} (\nu_E (\frac{\partial u_i}{\partial x_j} + \frac{\partial u_j}{\partial x_i})) &= \frac{\partial}{\partial x_j} (\nu_E \frac{\partial u_i}{\partial x_j}) + \frac{\partial}{\partial x_j} (\nu_E \frac{\partial u_j}{\partial x_i}) = \\
 &= \frac{\partial}{\partial x_j} (\nu_E \frac{\partial u_i}{\partial x_j}) + \frac{\partial \nu_E \partial u_j}{\partial x_j \partial x_i} + \nu_E \frac{\partial \partial u_j}{\partial x_j \partial x_i} = [\frac{\partial u_j}{\partial x_j} = 0] = \\
 &= \frac{\partial}{\partial x_j} (\nu_E \frac{\partial u_i}{\partial x_j}) + \frac{\partial \nu_E \partial u_j}{\partial x_j \partial x_i}
 \end{aligned} \tag{31}$$

The first term is discretized with central differences. The second term is discretized in a finite difference way with central differences and is added to the right hand side of the system.

The turbulent equations contain only the first term, which is treated in the same way as in the Navier-Stokes equations.

3.5 Gravity source term

A source balancing method is used to introduce gravity, Leveque (1998), Hubbard and Garcia-Navarro (1999). The body forces that arise from the gravity are incorporated into the approximate Riemann solver and the Roe type discretization. The pressure gradient due to gravity is subtracted from the input states for the solver. Thus, only the perturbations from the steady state are seen, not the large hydrostatic pressure gradient that would otherwise create spurious accelerations of the fluid particles due to strong coupling of pressure and velocity.

The constant value Q_i is replaced by two values Q_i^+ and Q_i^- with a jump δ at a cell centre, see Figure 8.

$$Q_i^+ = Q_i + \delta_i, \quad Q_i^- = Q_i - \delta_i \tag{32}$$

The introduced jump corresponds to the source term $\frac{\rho_i}{F_n^2} \Delta V_i$, representing the variation in pressure arising from the gravitational force.

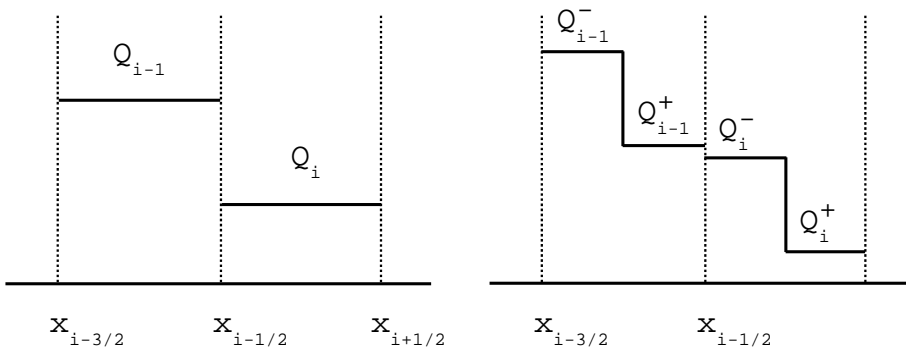


Figure 8: Data in two adjacent cells before and after introducing a jump in cell centres.

3.6 Initial and Boundary conditions

The boundary conditions are implemented using two layers of ghost cells. As mentioned in the previous chapter the OUTFLOW is modified as compared to a RANS code without free-surface capturing method. The Neumann condition is applied to the pressure in order to allow certain free surface level variation. Additionally a new boundary condition type is implemented here and referred to as the TOP and based on the standard SLIP boundary but with Dirichlet condition for the pressure. The TOP is used far from the disturbance of the hull where the pressure variation can be assumed negligible. Figure 9 illustrates the boundary conditions used for a typical flow domain.

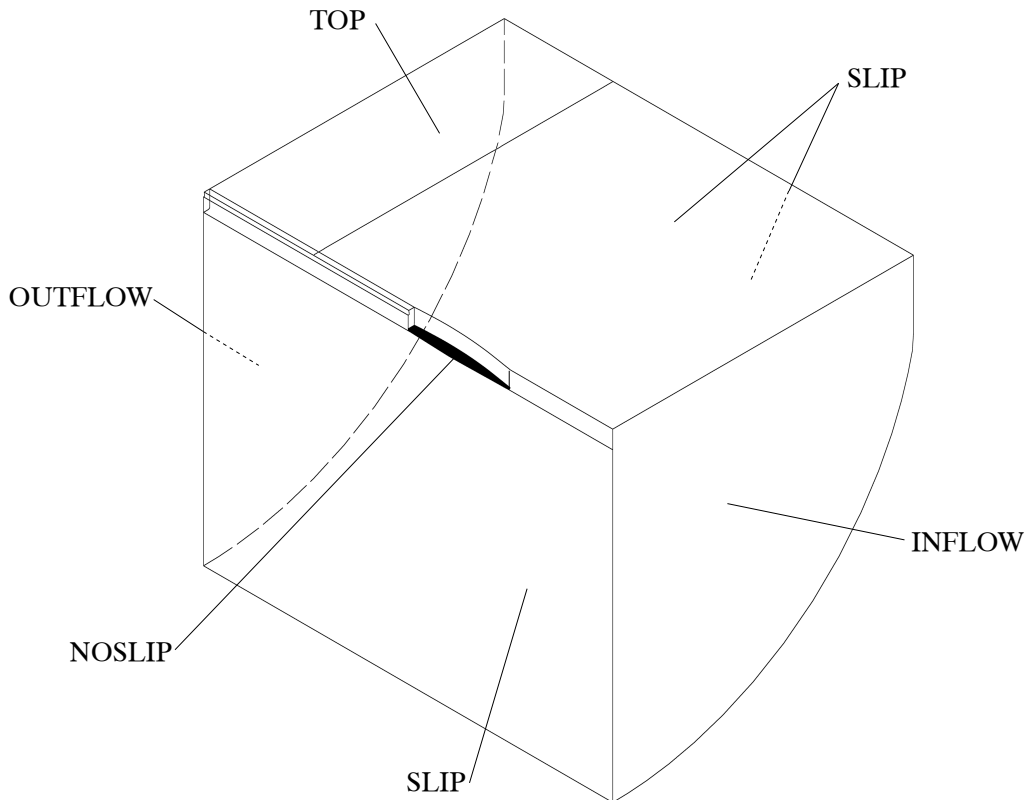


Figure 9: Boundary conditions.

The initial conditions are set to a uniform flow with an undisturbed free surface. The hydrostatic pressure and void fraction fields are prescribed accordingly. The initial guess for the velocity field is based on the Reynolds number and a boundary layer is introduced in the vicinity of the non-slip surfaces. A special consideration is made for ships with transom where a separated flow region is expected. There, the initial boundary layer is much thicker than on the other parts. This was found to improve the solver stability in the beginning of computations.

3.7 Solution Algorithm

A local artificial time-step is added to the equations and the discrete coupled equations are solved with the Alternating Direction Implicit (ADI) method. Since an acceleration of the flow velocity is not applicable due to the steady solver implementation, the pressure and velocities may change rapidly in the beginning of the calculations. This may cause instabilities of the free-surface and lead to solution divergence. The problem is addressed by introducing a start-up phase, where in order to stabilize the computations the fluid viscosity is modified. It was found that increasing the viscosity by three orders of magnitude and slowly decreasing it over several hundred iterations until it reaches the appropriate level resolves the initial instability issue.

A common problem with surface capturing methods used with RANS solvers without the wall function approach for a turbulence model is the necessity of using very thin cells close to non-slip boundaries. This leads not only to a slower convergence of the free surface location but also to a risk of drawing the air fraction under the hull. This is a major problem that causes a substantial error in resistance prediction. An extrapolation of the water fraction to the wall is used to efficiently resolve the issue, see Figure 10. A very small distance from the hull surface is affected by the procedure which has a limited influence on the solution and therefore is considered as a suitable treatment.

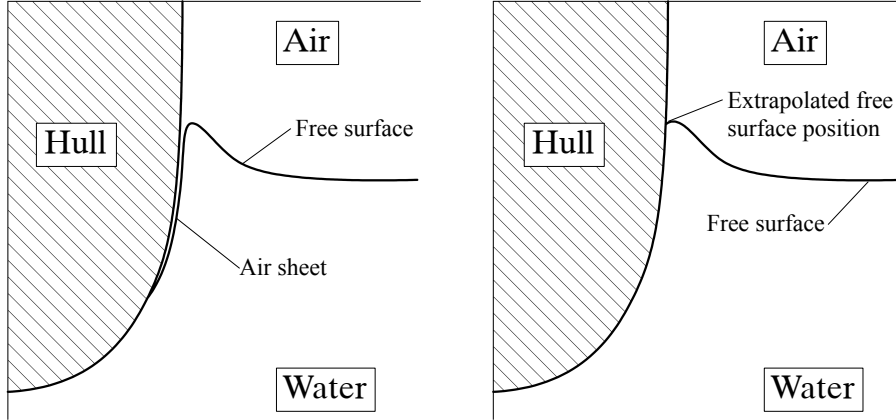


Figure 10: Example air sheet problem illustrated on a hull section. Without (left) and with (right) extrapolation. Schematic drawing, not to scale.

4 ADAPTIVE OVERLAPPING GRID REFINEMENT

The overlapping grid idea dates back to the early 1980s and has its roots at NASA Ames Research Center in USA. More often it is called overset or Chimera grids and the development officially began in 1983 when Steger, Dougherty and Benek presented a general framework for Chimera grids, Steger et. al. (1983). The major driving force for this approach was an ability to use good quality structured grids on complicated geometries and to have a possibility to apply relative motions between components in a flexible way without regridding the computational domain. An additional advantage is also that the parts of the geometry can be modified, repositioned, added or removed with small effort.

The major difficulty for the overlapping algorithm is usually an intergrid boundary definition. Two approaches can be distinguished that address this issue. The first is priority based where each component grid is assigned a value that specifies which grid cuts hole in the other grid. This approach is utilised in the very well-known PEGASUS and SUGGAR codes, Noack (2005). It is widely used for aeronautical, and recently marine applications Carrica (2005). The second approach is using a local distance function to set the boundaries. At least two independent groups have been working on that method: Nakahashi (2000), unstructured grids for multiple moving-body aeronautical problems and Regnström (2000), structured grids for local refinements and appendages for marine applications.

Overlapping grid techniques are usually introduced in order to compute the flow around complicated geometries without compromising cell quality. This technique was already used in SHIPFLOW at the start of this project. It may be used to describe the geometry or to refine locally the grids in the domain regions that require higher spatial resolution. In the present work the latter application is incorporated in the near free surface region to avoid excessive wave damping and to increase the interface sharpness. Additionally the refinement grid can be automatically adapted to the wave profile, which allows to reduce the size of the refined region and also further decreases the air-water transition band thickness.

A background grid describes the computational domain extent and can also represent the main geometry features, while the component grids add more details to the geometry or increase the grid resolution. The grids overlap each other and the communication between them is realized by interpolation. A principle of the overlapping grid set up is shown in Figure 11.

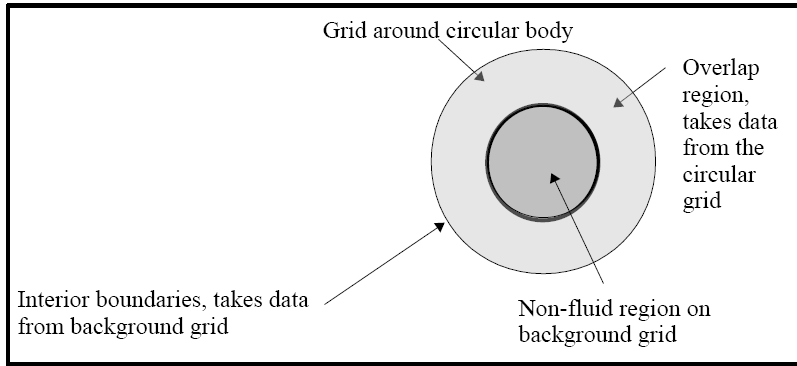


Figure 11: Overlapping grids principle.

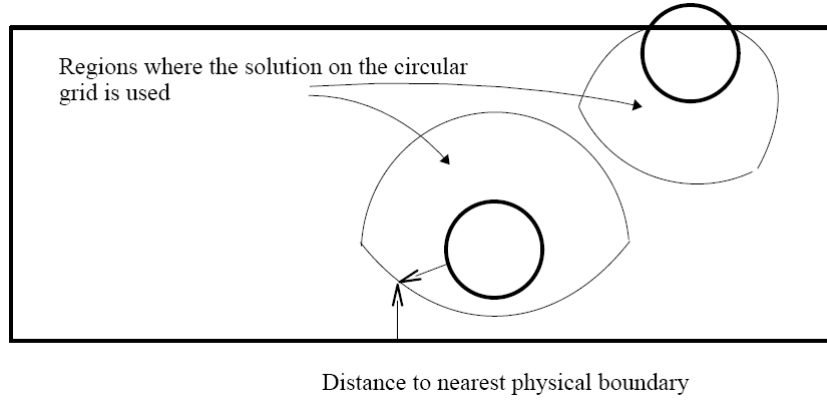


Figure 12: Distance function based overlapping grid algorithm.

The major difficulty is to decide upon which way to interpolate i.e. which grid to be used to represent the flow. As mentioned already the algorithms differ considerably between codes. In most reported overlapping methods priorities are assigned to each component thus creating hierarchical structure. In the current framework, however, a local distance function criterion is used, see Figure 12. The distance function is equal to the shortest distance to the physical boundary represented by the grid. In the overlapping regions the FB is compared at each cell centre and the one with smaller value is selected. This method proved to be robust and requires little user input.

In the method developed by Regnström, (2007), for each component grid in the calculated case the overlapping algorithm follows the procedure below:

- Set up interpolation information for periodic, folded and multi block interfaces.
- Calculate the local distance function FB.
- Find interpolation information between grids that overlap.
- Correct boundary mismatch in regions where two grids represent the same surface.

- Flag cells that are outside the domain as non-fluid.
- Trim double interpolations to avoid circular dependence

For the free surface flows the core technology of the overlapping algorithm is utilized and extended further to handle the complications implied by the new application. A new standard component grid is added for free surface refinement. A rectangular grid is created around the air-water interface with a hyperbolic grid generator. The isosurface of the air volume concentration equal to 0.5 is used first to create the surface mesh, then the refinement grid grows above and below the interface. The water level is then followed and the refinement is recreated when the wave amplitude change exceeds a given criterion. In order to keep the interface inside the refined region the criterion is set usually to 2-3 cell heights. Specifying smaller values would help to adapt the grid more accurately but too frequent updates may take time and also slow down convergence. A flowchart of the implemented adaptation algorithm is illustrated in Figure 13. First the grids are imported or generated by the integrated grid generation tool and the overlapping algorithm is executed and interpolation information computed. Thereafter, the solver is started and the adaptation criterion is checked every 10th iteration. When the wave amplitude change is sufficiently large the refinement grid is adapted to the free surface shape. The overlap and interpolation information are set up after each adaptation and the solver continues until convergence.

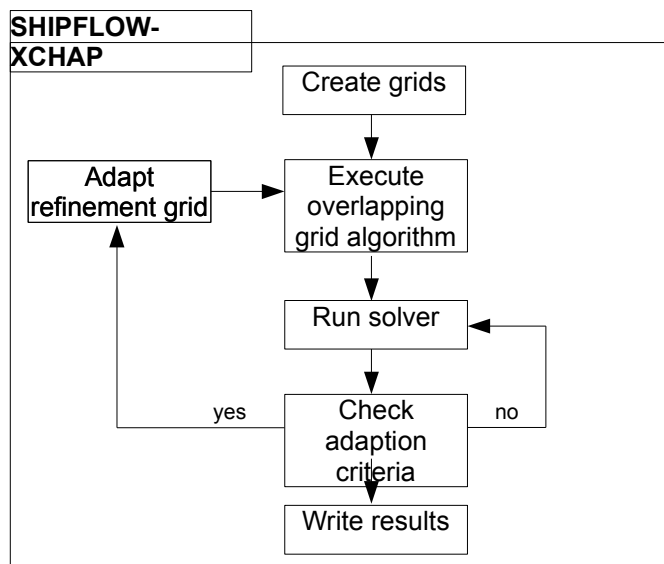


Figure 13: Program flow chart with adaptation loop.

The refinement may cover the whole free surface or only a part, increasing solution accuracy in the region of interest, and creating wave damping zones near

domain boundaries. An example grid assembly is shown in Figure 14. A submerged hydrofoil component grid is placed in a much coarser background grid. A part of the free surface is refined with additional component grid, which can be adapted to the waves. The adapted grid for the converged solution is shown in Figure 15.

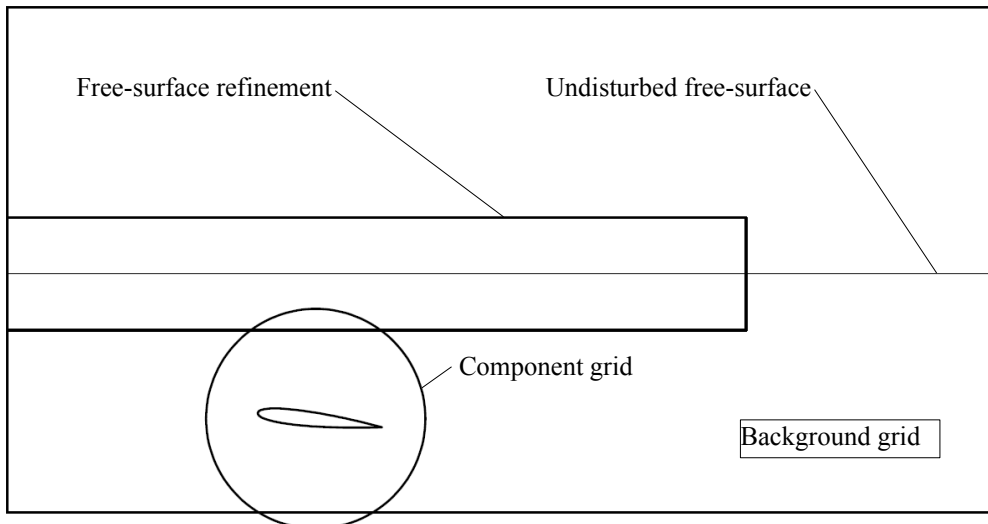


Figure 14: Overlapping grid arrangement with free surface refinement.

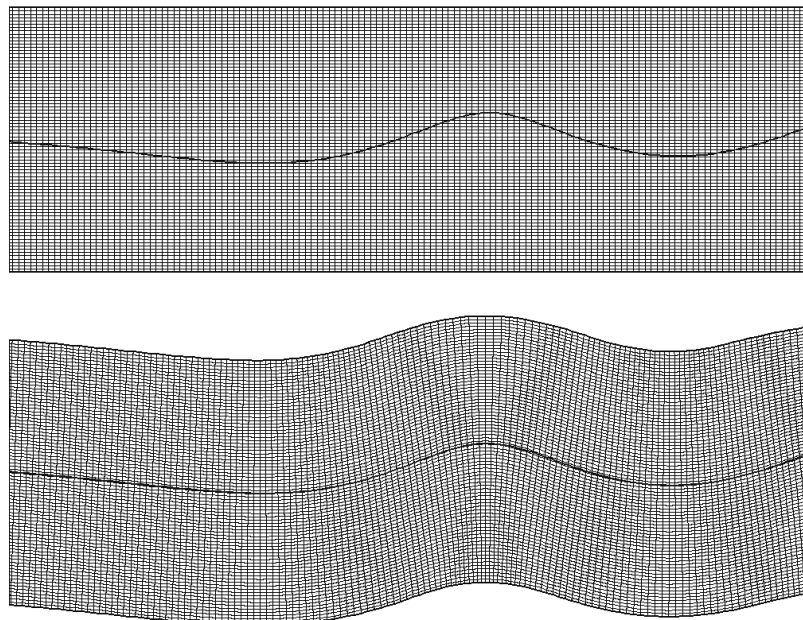


Figure 15: Result of calculations with overlapping grid fixed and adapted to the free surface profile.

5 CASE STUDIES

Four different test cases are used for the free surface flow code verification and validation. The investigation starts with looking at effects of discretization of the volume fraction equation and effects of the overlapping grid refinement of the air to water interface. For this purpose a 2D case of submerged hydrofoil, the Duncan test case, and the Series 60 ship hull are used. A number of discretization schemes are applied to illustrate an importance of the convection part discretization on the free surface sharpness. A verification and validation is carried out for the Wigley hull as well as the KRISO Container Ship, KCS. The results are compared with the available measurements. The verification is performed with Least Squares Root Method as described in Eça and Hoekstra, (2006).

5.1 Submerged hydrofoil test case

5.1.1 Case description

The first test setup corresponds to the experiments carried out by Duncan (1983). A hydrofoil with a NACA 0012 section and a chord length of 0.203 m was placed in a towing tank with a total depth of 0.385 m. The tank was 0.610 m wide and the span of the hydrofoil was 0.600 m which, due to a very small gap between the foil tips and the tank walls, allowed to disregard the three-dimensional effects. For the current simulations a case where no wave breaking occurred was selected. The submergence for this conditions was 0.210 m and the angle of attack was 5 degrees. The towing carriage speed was 0.8 m/s which corresponded to the Froude number of $F_n=0.567$ and the Reynolds number of about $R_n=1.6*10^5$ based on the chord length.

5.1.2 Computational setup

This test case is computed as two-dimensional and the grid is composed of three structured overlapping components with quadrilateral panels, similar to that shown in Figure 16. A relatively coarse regular background grid determines the extent of the computational domain, which is 2 chord lengths upstream and 16 downstream of the hydrofoil leading edge. The height is 4 chord lengths. The background grid has only 1800 cells. The hydrofoil section is represented with a boundary fitted curvilinear component grid generated with a conformal mapping method and has 1000 cells. The outer edge of this component is nearly circular with a radius of about 1 chord length. In order to improve the results with a minimal computational cost, a thin, local refinement grid is placed around a part of the air and water interface. The thickness is chosen such that the height of the refinement is larger than the expected wave amplitude, and the refinement starts at the inlet boundary of the background grid and extends 7 chord lengths downstream of the hydrofoil's leading edge. It is symmetrical above and below the free surface. The remaining length, downstream to the domain outflow boundary, is used for wave damping to avoid reflections from the downstream

boundary. The refinement has 24000 cells and is either a regular type or a boundary fitted adaptive curvilinear grid with a middle layer conforming to the computed instantaneous free surface shape. The cell size in the refined region is 0.01 and 0.03 chord lengths in the vertical and longitudinal direction respectively. For the given conditions there are 66 cells per wave length and the wave amplitude is around 15 cells. The calculations are carried out using the $k-\omega$ SST turbulence model at R_n according to the experimental set up. In all cases the CFL number is reduced to 0.2 in order to minimize the risk of instabilities that may occur for some of the more compressive discretization schemes.

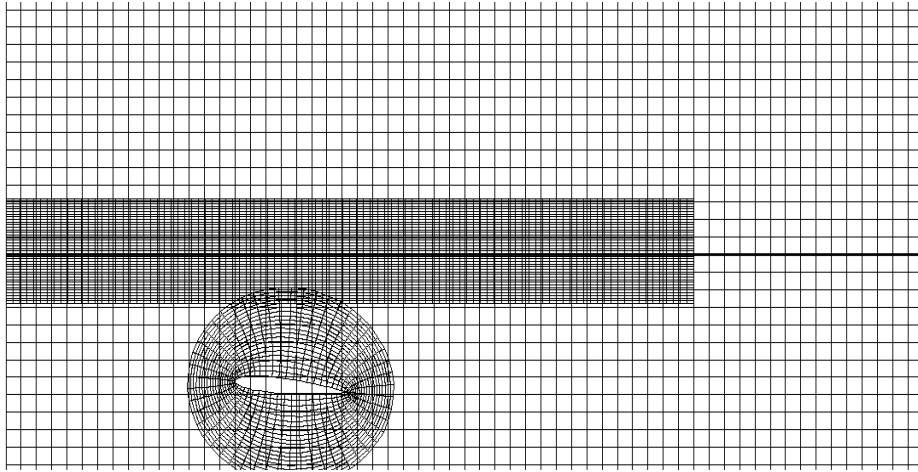


Figure 16: Computational grid for Duncan case with refinement.

The result of computations with the Superbee scheme and measured wave profiles are shown in Figure 17. The agreement is good in general, the wave phase is correct, however the amplitude is underestimated. The reason for this is the very coarse background and hydrofoil grids which is influencing the accuracy of the pressure computations. This difference is however insignificant since the emphasis in the present investigation is the interface sharpness.

Wave profile for Duncan test case with depth of submergence=21 cm

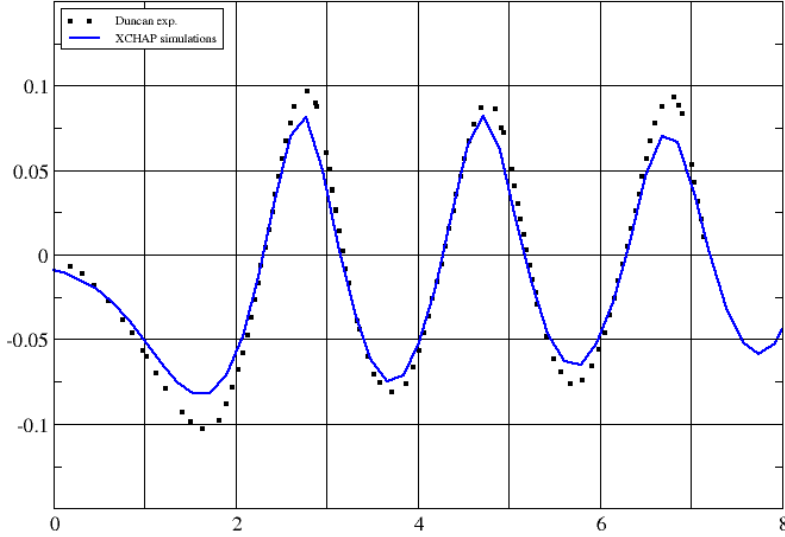


Figure 17: Measured and computed wave profiles comparison.

5.1.3 Effects of discretization scheme

The interface thickness with a fixed grid varies from about 14 to 3 cell thicknesses for the investigated schemes, see Table 1. The estimate is done in the trough downstream of the first wave behind the hydrofoil.

Scheme	Interface thickness	
	Fixed refinement	Adaptive refinement
MinMod	14.5	6.5
Osher	9.0	5.5
MUSCL	7.0	4.8
SuperBee	4.8	4.2
SuperBee-C	3.9	3.9
Hyper-C	3.4	3.4
STACS	2.9	2.9

Table 1: Approximate interface thickness in cells, measured between water fraction isolines of 0.01 and 0.99.

Figure 18 illustrates the first wave behind the submerged hydrofoil. The water fraction isolines of 0.01, 0.5 and 0.99 are shown. The interface is considerably

smeared out for the MinMod and the wave crests tend to break due to increased wave slopes in the low water fraction part of the transition band. This case was not iterated until convergence but rather stopped just before the breaking occurred. A visible reduction of the interface thickness is achieved with the Osher and further with the MUSCLE schemes. The interface band is reduced by about 50% compared to the MinMod and is more uniform along the wave train. No problems with breaking were observed. The compressive schemes bring a significant improvement compared to the other solutions. The Superbee gives thickness just below 5 cell heights which is already a satisfactory result. Even greater decrease of the interface thickness was achieved with the Hyper-C. However, a staircase like wave profiles can be recognized due to an alignment of the interface with the grid lines, see also Orych et al. (2009). A remedy for that is to use blended schemes such as STACS which was also investigated. It performs very well in terms of keeping the interface thin; achieved result was 2.9 cells across. However, the computations are a bit slower compared to other schemes described here due to its more complex implementation. The proposed SuperBee-C scheme, which is an intermediate solution between SuperBee and Hyper-C gives interface thickness of 3.9 cells. This is one cell less than the SuperBee but still the staircase like wave contours are not visible.

The wave height is nearly the same for all schemes even though the air to water transition band differs significantly. The MinMod is excluded from the comparison for the reasons mentioned earlier. A very interesting observation is made about the wave length. The results are consistent except for the Hyper-C and STACS, also based on the Hyper-C, where the wave length is about 10% larger compared to the other schemes.

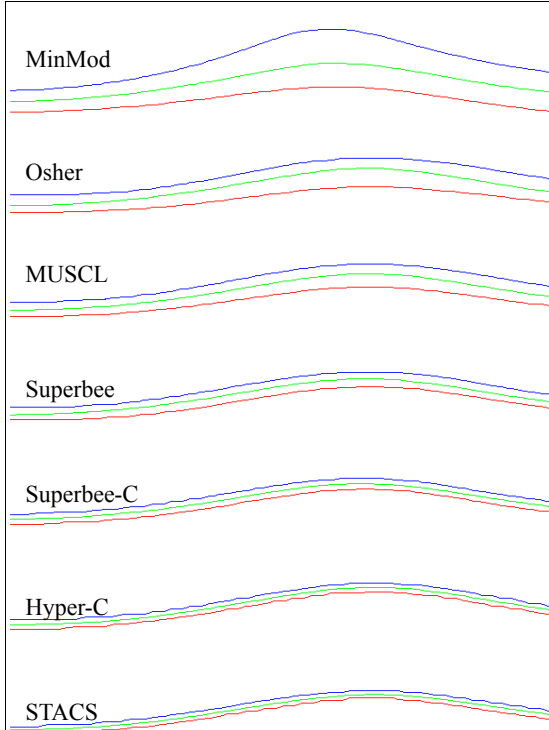


Figure 18: Interface thickness comparison without refinement adaptation for various discretization schemes illustrated on the first wave crest. The water fraction isolines of 0.01, 0.5 and 0.99 are shown in blue, green and red respectively.

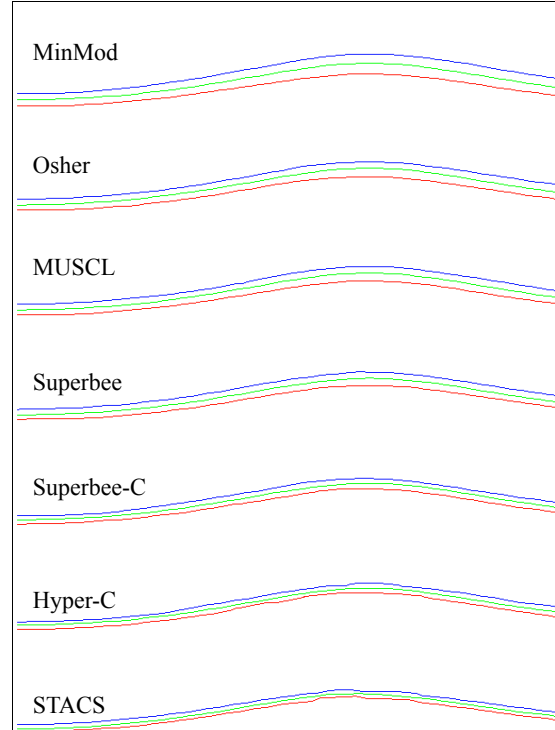


Figure 19: Interface thickness comparison with refinement adaptation for various discretization schemes illustrated on the first wave crest. The water fraction isolines of 0.01, 0.5 and 0.99 are shown in blue, green and red respectively.

5.1.4 Effects of overlapping refinement

The second objective of the work was to investigate the adaptive grid refinement effects on the solution. The interface thickness comparison with the adaptive refinement for various discretization schemes is illustrated on the first wave crest, Figure 19. The alignment of the grid lines with the free surface profile decreases the interface diffusion considerably for the non-compressive schemes. A reasonable thickness was even achieved for the MinMod. The observed thickness reduction was in this case over 50% compared to the case computed with the fixed grid with the same cell size, see Table 1. A large reduction was also achieved for the Osher and MUSCL scheme and was about 40% and 30% respectively. The improvements decrease as the discretization schemes are less diffusive. The Superbee shows only a slight change while the Superbee-C, Hyper-C and STACS do not indicate any noticeable change in the interface thickness. However, since the grid lines are aligned with the free surface the stair case phenomena do not appear for the highly compressive schemes as was the case for the fixed grid.

5.2 Series 60 test case

The Series 60 ($CB=0.6$) hull is chosen as the second test case. The results are compared to the measurements of Toda et al. (1992). The selected measurements are performed with a 3.048 m long model at a Froude number of 0.316 and a Reynolds number of 5.245×10^6 . A bare hull is considered in model-fixed conditions, without effects of dynamic sinkage and trim.

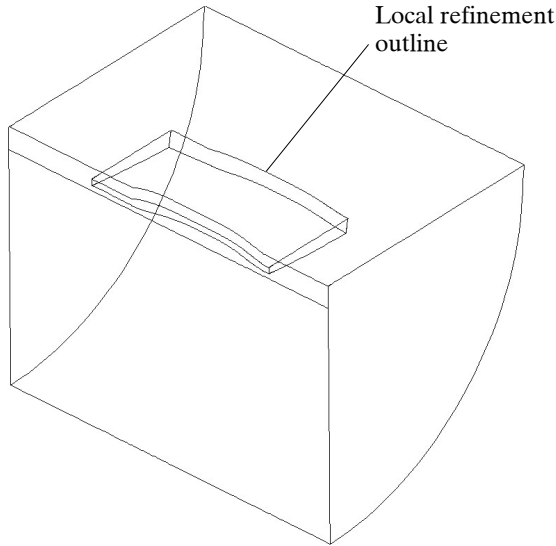


Figure 20: Background grid with a local free surface interface refinement near the hull.

5.2.1 Computational setup

The computations are carried out with two grid sets, without and with refinement. For the case without a refinement a single-block grid with H-O topology is used. The computational domain extends 0.5 length between perpendiculars (Lpp) upstream of the forward perpendicular and 1.0 Lpp behind the aft perpendicular. The outer boundary has a radius of 2 Lpp and the top is 0.1 Lpp above the water plane. The cells are stretched in the normal direction to the hull to satisfy requirements of the turbulence model. In the vertical direction the grid is refined close to the free surface, where the cells had the thickness $\Delta z = 0.00175$ Lpp. Along the hull there are 82 cells with stretching applied near the bow and stern. The cell length Δx varies between 0.01 and 0.018 which corresponds to 62 and 35 cells per wave length. Behind the hull the cell size increases for wave damping purposes to avoid reflections from the outlet and therefore the waves become less pronounced shortly behind the transom. In total only 590 000 grid cells are used. The grid is relatively coarse in order to emphasize the effects of the discretization schemes and the grid refinement.

The second grid setup is created by adding a local refinement of the air-water interface around the hull, Figure 20. It starts 0.05 Lpp in front of the bow and ends 0.35 Lpp behind the stern. The transverse extent is 0.65 Lpp and covers the

wave pattern at the whole length of the hull. The refinement spreads 0.18 and 0.17 above and below the undisturbed free surface level. In each direction the cell number is doubled in this volume giving 950 000 additional cells. All simulations are performed with the CFL number of 0.5 for stability reasons. Figure 21 illustrates the wave patterns from the grid with a refinement, top part, and the measured one, bottom part. Considering the limited grid resolution the results show a good agreement with the measurements. There is a small difference in the wave length and amplitude due to the numerical diffusion, however the wave pattern characteristic features can be recognized.

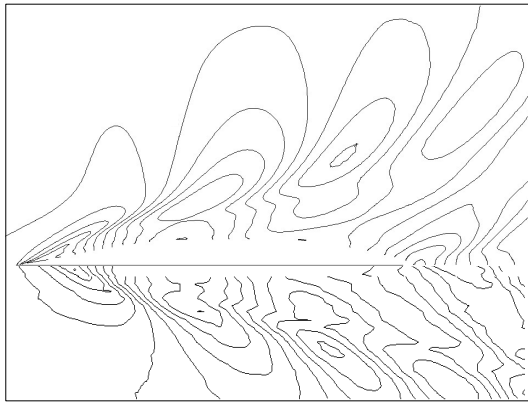


*Figure 21: Wave pattern comparison, top:
CFD, bottom: measurements. Spacing
between contour lines 0.0025 L.*

The next two subsections deal with the discretization scheme and refinement influence on the results. In both cases 2D wave profiles in longitudinal and transverse planes are used to check the interface thickness. Selected parts of the wave profiles are visualized with 0.1, 0.5 and 0.9 isolines of the water fraction.

5.2.2 Effects of discretization scheme

The wave patterns computed with Superbee-C and MUSCL are illustrated in Figure 22. There is a very small difference between the contour lines. It was already observed in the Duncan case that the discretization scheme mostly influenced the interface thickness, while the wave profiles were nearly the same. The wave pattern as a three-dimensional wave amplitude distribution shows the same trend. The most visible difference can be observed looking at the diverging bow waves which seem to be damped more when the MUSCL was used.

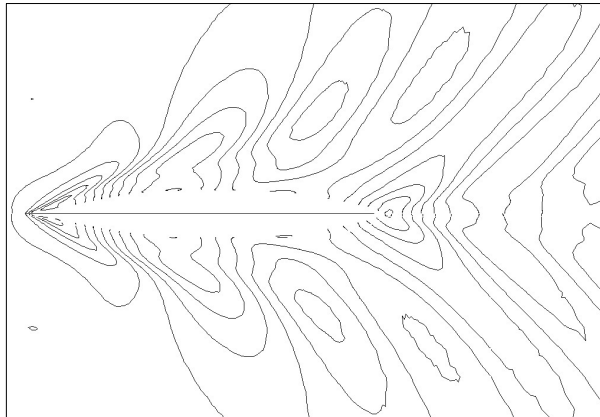


*Figure 22: Wave pattern comparison, top:
SuperbeeC, bottom: MUSCL. Spacing
between contour lines 0.0025 L.*

A longitudinal cut at 0.08 L_{pp} from the center plane and a transverse cut at 0.1 L_{pp} downstream of the forward perpendicular, shown in Figures 23, 24 and 25, include results of three discretization schemes: MUSCL (green lines), Superbee (blue) and Superbee-C (red). In all cases the wave amplitude has been scaled by a factor of five for better picture clarity. The contour lines of the water fraction of 0.5 coincide with each other for all schemes in the major part of the wave profile. The exceptions can be found in the bow wave crest where the Superbee-C predicts a little higher peak, see Figure 23 and 25. An air-water transition band thickness reduction of about 30% can be observed along the hull comparing the MUSCL and Superbee-C methods.

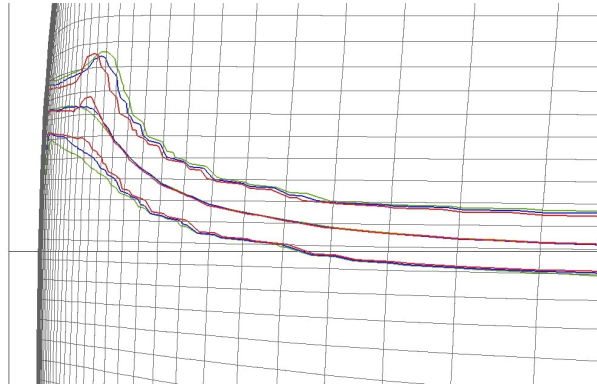


*Figure 23: Water fraction contour lines at
the transverse plane located 0.1 L_{pp}
downstream of forward perpendicular.*

Looking at the whole wave pattern it is noticeable that the interface thickness in case of the MUSCL scheme is increasing in the downstream direction and also the wave amplitude is reduced further away from the hull. The Superbee and Superbee-C maintain the interface thicknesses and the waves are less damped.

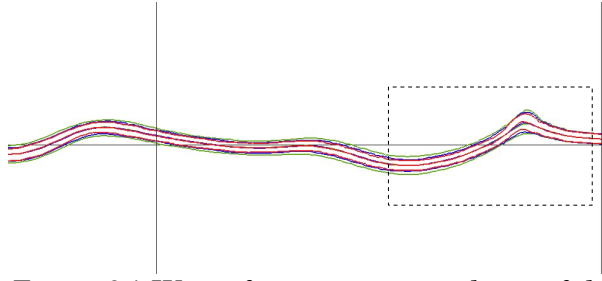


Figure 24: Water fraction contour lines of the longitudinal wave cut at $0.08L_{pp}$ off the center plane. The water fraction isolines of 0.1, 0.5 and 0.9 are shown for MUSCL (green), Superbee (blue) and Superbee-C (red).

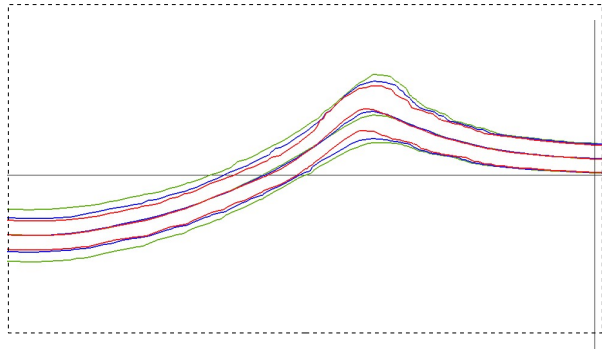


Figure 25: Close up of the water fraction contour lines near the bow. The water fraction isolines of 0.1, 0.5 and 0.9 are shown for MUSCL (green), Superbee (blue) and Superbee-C (red).

In the transverse cut the computational grid lines are included for better understanding of the interface thickness relative to the cell size, Figure 23.

5.2.3 Effects of overlapping refinement

The computations with a grid refinement are illustrated on a case for which the Superbee scheme was used. The grid adaptation implementation has not yet been finalized in 3D, since several important issues were discovered which were not posing problems in the 2D example. There are two major difficulties in this case: treatment of the near wall region and interpolation from the background grid to the refinement grid upstream of the hull.

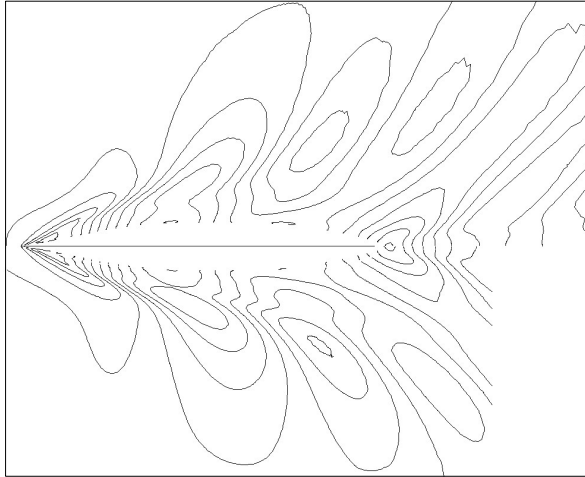


Figure 26: Wave pattern comparison, top: no refinement, bottom: with refinement. Spacing between contour lines 0.0025 L .

Using an adaptive grid that is not fitted to the hull causes difficulties in the near wall region where the refinement grid intersects the hull surface. In this region the interpolation of the solution from the body fitted grid, describing the hull, to the adaptive refinement is necessary. Since the cell size and the aspect ratio changes rapidly the information about the flow field received by the refinement is of a coarse quality. Several attempts have been made to compute such cases but the results were not satisfactory. Therefore, a conclusion has been made that the adaptive grid should be body fitted and slide on the hull surface in order to take full advantage of the method.

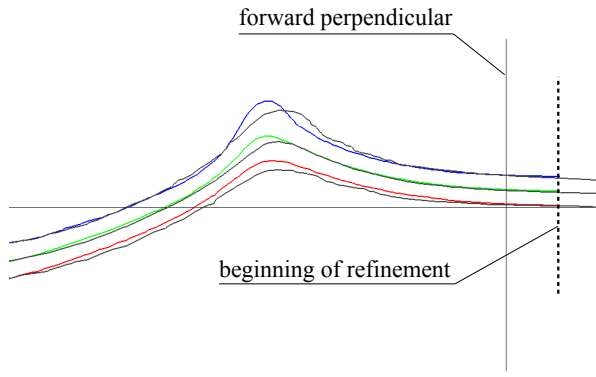


Figure 27: Close up of the water fraction contour lines near the bow, with and without refinement. The water fraction isolines of 0.1, 0.5 and 0.9 are shown for the refined region in blue, green and red colors respectively. The isolines for the grid without the refinement are indicated with black lines.

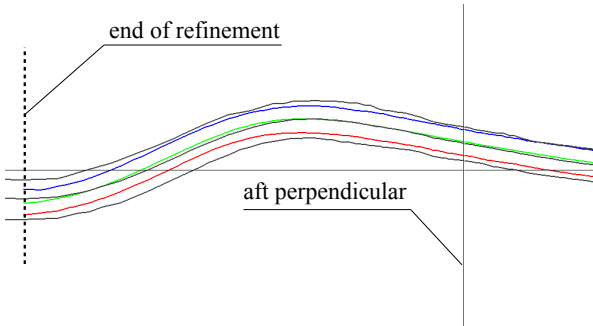


Figure 28: Close up of the water fraction contour lines near the stern, with and without refinement. The water fraction isolines of 0.1, 0.5 and 0.9 are shown for the refined region in blue, green and red colors respectively. The isolines for the grid without the refinement are indicated with black lines.

The results presented here are based on a fixed body fitted refinement. A comparison of the wave pattern without and with the refinement is shown in Figure 26. An improvement in contour details and an increased wave amplitude of the diverging waves are clearly visible. The longitudinal wave cuts shown in Figures 27 and 28 cover only a bow and a stern regions including the ends of the refinement. Thin lines indicate the hull ends and the still water plane level. Thick dashed vertical lines indicate the beginning and end of the refinement. The black solid contour lines which continue across the whole width of the pictures belong to the computation without the refinement and the blue, green and red are water fraction contours are computations with the refinement. The information about the thick interface coming from the upstream, coarse part of the domain is interpolated into the refinement and acts as a bad quality, with respect to the interface sharpness, inflow boundary condition. This is then convected downstream and only a small reduction of the thickness can be noticed. This is due to the finer grid used for solving the flow. However, the advantage of using the refinement is not fully utilized. A method for passing the information about the free surface location which would not include the interface thickness or compress it quickly where the interpolation is towards the finer grid should be developed. Extending the refinement up to the domain inlet is possible and was made in 2D case, however a considerable amount of cells would be added.

5.3 Wigley test case

The Wigley hull form is still widely used for viscous free surface code verification and validation due to its simple geometry and exact mathematical description. The slender body and V-shaped sections allow for easy grid generation using various grid topologies ranging from H-H to O-O type. There is a large amount of experimental and computational data available for validation and comparisons

which makes the case very attractive for the first real hull simulations.

In this test the hull is fixed, no trim or sink allowed, sailing at a Froude numbers of 0.250 and 0.316 with corresponding Reynolds numbers of 5.57×10^6 and 7.04×10^6 which follows the tests performed at SRI, see Kajitani et al. (1983).

5.3.1 Computational setup

A structured H-O topology grid was used. The computational domain extends 1.0 Lpp upstream of the hull, 2.0 Lpp downstream, 3.0 Lpp to the side and below and 0.15 Lpp above the undisturbed free surface level.

In total, seven systematically varied, geometrically similar grids are generated applying a grid refinement ratio of $\sqrt[4]{2}$ in the three directions of the domain: longitudinal, circumferential and radial. The number of grid cells and the relative grid cell sizes are given in Table 2. The grids are stretched in longitudinal direction with cell concentration near bow and stern. The size increase upstream of the bow and downstream of the stern. In the normal direction to the hull the grids are stretched towards the hull surface and the spacing close to it varies from $y+=0.7$ up to 1.98 for the finest and coarsest grid respectively. The large cell size away from the hull is used to limit amount of cells and also to create a wave damping zone to avoid reflections from the boundaries. In order to capture the free surface interface accurately the grid is stretched towards the still water plane. The spacing in the vertical direction is 5×10^{-4} Lpp for the finest grid and the refined zone extends 0.015 Lpp above and 0.005 Lpp below the water plane to cover the free surface waves. The computations are carried out with Superbee discretization scheme.

Grid	Cells (1e6)	h/h_i ($i=1, 2, \dots, 7$)
G1	9.91	1.000
G2	5.89	1.189
G3	3.50	1.414
G4	2.08	1.682
G5	1.24	2.000
G6	0.74	2.378
G7	0.44	2.828

Table 2: Grid sequence for the Wigley hull.

5.3.2 Results – resistance

The results obtained with the code including total resistance coefficient as well as pressure and frictional components are presented in Table 3 and 4. The tables contain also values extrapolated to zero grid cell size and the measured total resistance coefficient. The grid convergence is investigated using the Least

Squares Root approach (Eça and Hoekstra, 2006). As can be seen the total resistance coefficient values extrapolated to zero grid size show an extremely small deviation from the measurements of about 0.2% for both Froude numbers.

	Exp.	G0	G1	G2	G3	G4	G5	G6	G7
C_F	-	3.26	3.21	3.20	3.20	3.14	3.10	2.95	2.71
C_P	-	0.93	0.96	0.95	0.94	0.95	1.01	1.04	1.07
C_T	4.20	4.19	4.18	4.16	4.14	4.10	4.11	3.99	3.79

Table 3: Measured and computed results including values extrapolated to zero cell size, $F_n = 0.250$. (All results multiplied by 1000.)

	Exp.	G0	G1	G2	G3	G4	G5	G6	G7
C_F	-	3.16	3.12	3.12	3.10	3.04	2.97	2.83	2.60
C_P	-	1.65	1.67	1.67	1.67	1.69	1.71	1.75	1.79
C_T	4.80	4.81	4.79	4.79	4.77	4.73	4.69	4.59	4.39

Table 4: Measured and computed results including values extrapolated to zero cell size, $F_n = 0.316$. (All results multiplied by 1000.)

The grid convergence is monotonic, however the observed order of accuracy, p , exceeds the theoretical one. This, most probably, is due to the fact that the coarsest grids are too coarse to give satisfactory solution. After removing the coarsest grids from the curve fitting the results are more realistic and are between two and three. The full result of the verification calculations is presented in Table 5. The comparison error E is defined as a difference between the simulation results for the finest grid S and the experimental data D . The solution change between two finest grids is denoted as ε_{12} . Both E and ε_{12} are very small, however the iterative error U_I indicates that the number of iterations for the finest grids should have been increased to consider this error as negligible in the uncertainty estimation, Zou and Larsson, (2013). The numerical uncertainty U_{SN} is very low at a level about 3% of the results extrapolated to zero grid size. The Figures 29 and 30 illustrate grid convergence with least square fit curve. A scatter that can be noticed is relatively small. A formal validation cannot be carried out due to lack of the experimental data uncertainty.

F_n	$E\%$	$\varepsilon_{12}\%$	p	$U_I\%$	$U_{SN}\%$
0.250	0.48	0.46	2.78	0.77	3.14
0.316	0.31	0.00	2.92	0.05	3.05

Table 5: Results of uncertainty analysis for C_T .

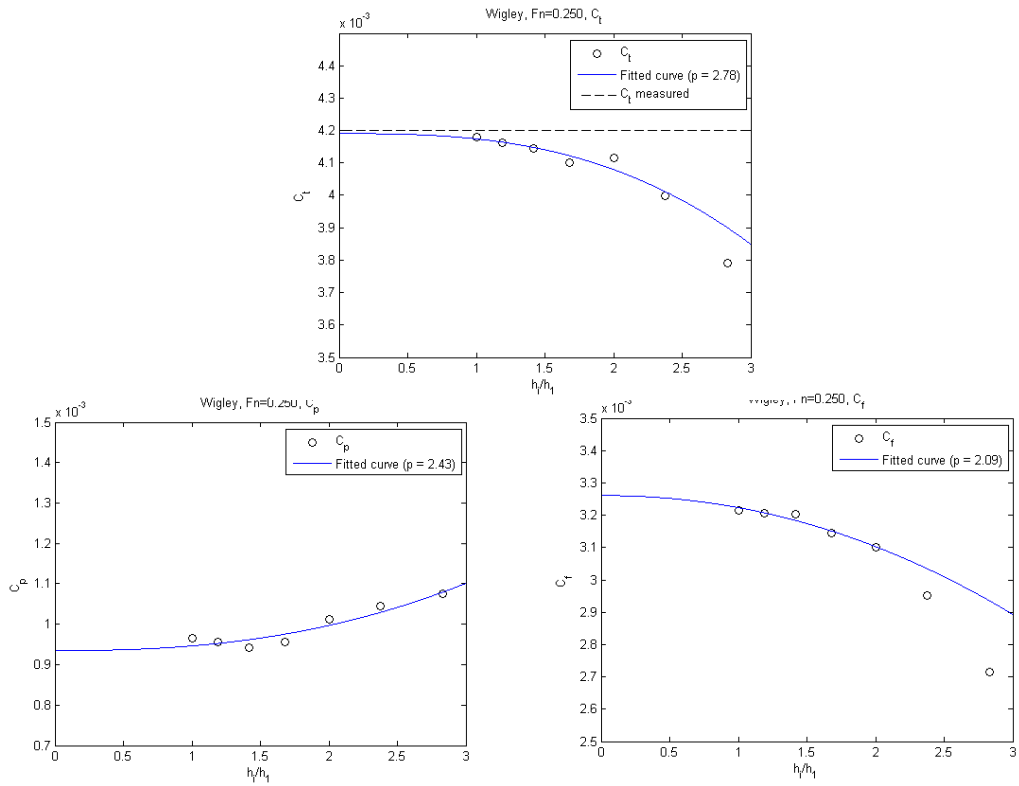


Figure 29: Grid convergence of C_T , C_P and C_F at F_n of 0.250.

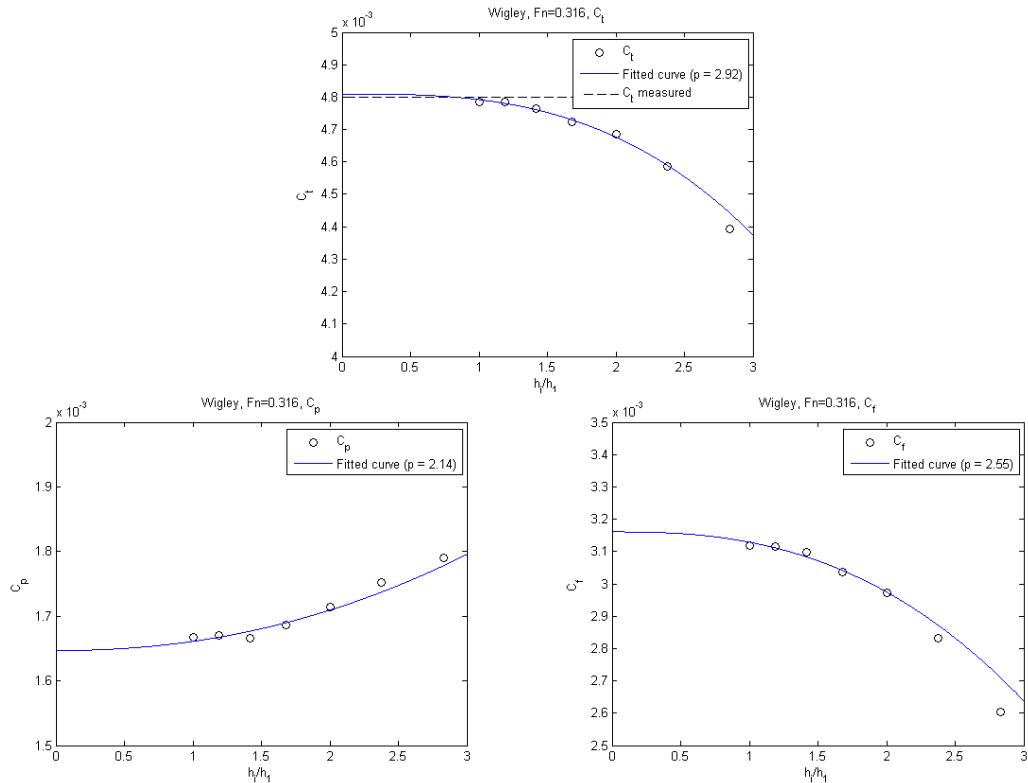


Figure 30: Grid convergence of C_T , C_P and C_F at F_n of 0.316.

5.3.3 Results – wave pattern

To evaluate the free-surface code a wave profile along the hull is compared to the measurements. Figures 31 and 32 illustrate the wave elevation for two Froude numbers. There are small deviations from the experimental data, however the agreement can be considered as good. The wave pattern, Figure 33, shows little wave damping even in the regions further away from the hull.

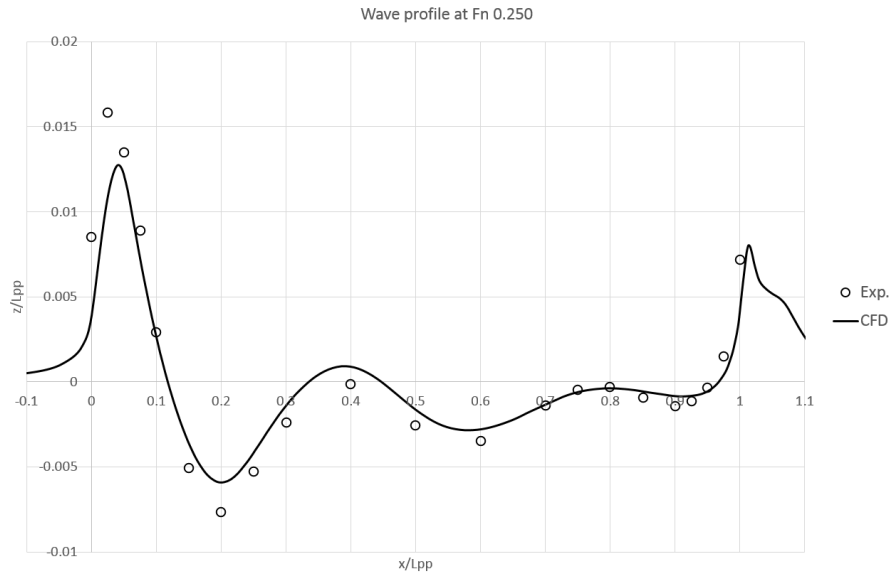


Figure 31: Computed and measured wave profile, $F_n = 0.250$.

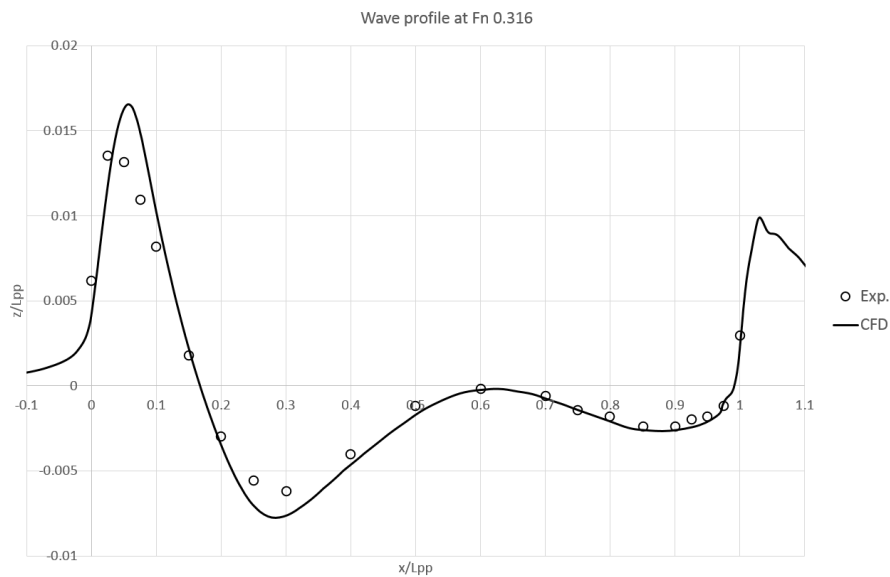


Figure 32: Computed and measured wave profile, $F_n = 0.316$.

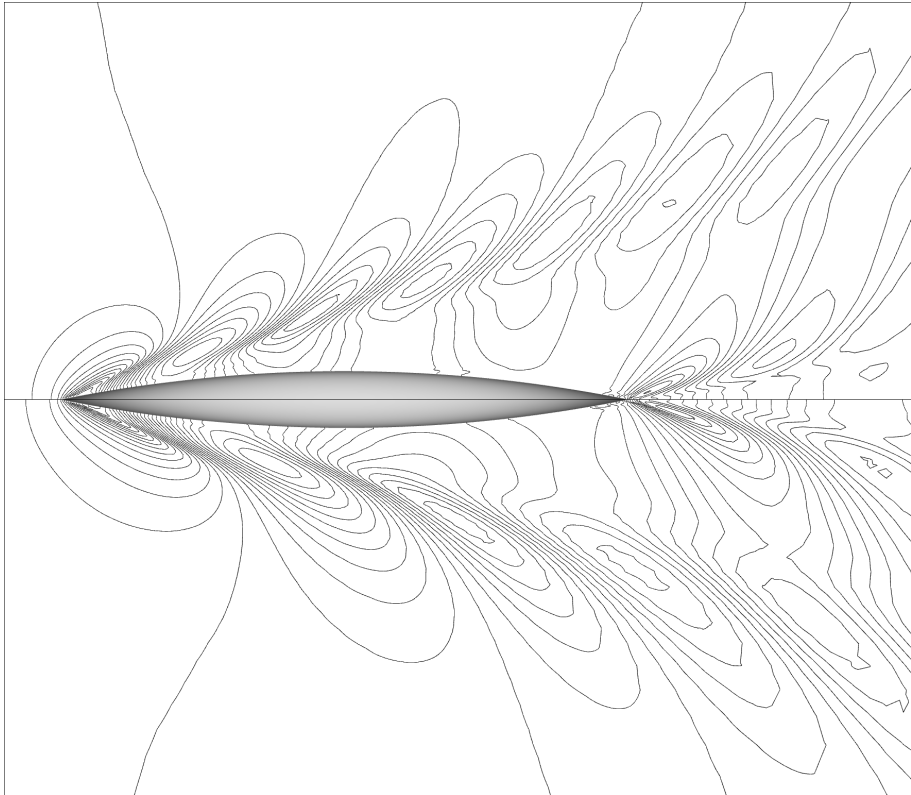


Figure 33: Wave pattern at $F_n=0.250$ (top) and 0.316 (bottom), contour spacing 0.001 .

5.4 KRISO Container Ship test case

The final test case is the KRISO Container Ship, KCS, which was designed in the mid '90s for validation purposes. Even though there is no full scale ship built, it represents a typical container vessel hull form with a bulbous bow.

The validation data originates from the experiments carried out at MOERI, see Kim et al (2001). In this study the Froude number was 0.26 and the corresponding Reynolds number was 1.4×10^7 . A bare hull was considered in model-fixed conditions, without effects of dynamic sinkage and trim.

5.4.1 Computational setup

The computations are carried out with structured, H-O type multi-block grid, Figure 34. One block constituted the main part and covers the whole hull except the volume behind the flat transom where an additional block is fitted. The domain extends 1.0 length between perpendiculars (Lpp) upstream of the forward perpendicular and 2.0 Lpp behind the aft perpendicular. The outer boundary has a radius of 3.0 Lpp and the top is about 0.15 Lpp above the water plane. The cells are stretched in the normal direction to the hull down to $y+ \sim 1$, varying with grid size, in order to satisfy requirements of the turbulence model.

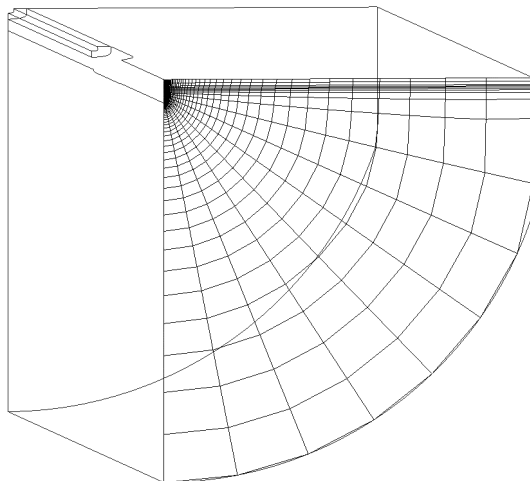


Figure 34: Multi-block, H-O volume grid with visible surface mesh at the inlet (grid was coarsened for the picture clarity).

In the vertical direction the grid is refined close to the free surface and the cell faces are aligned with the undisturbed free surface for the grid layers in the range from -0.01 to 0.015 Lpp in the z-direction, see Figure 35.

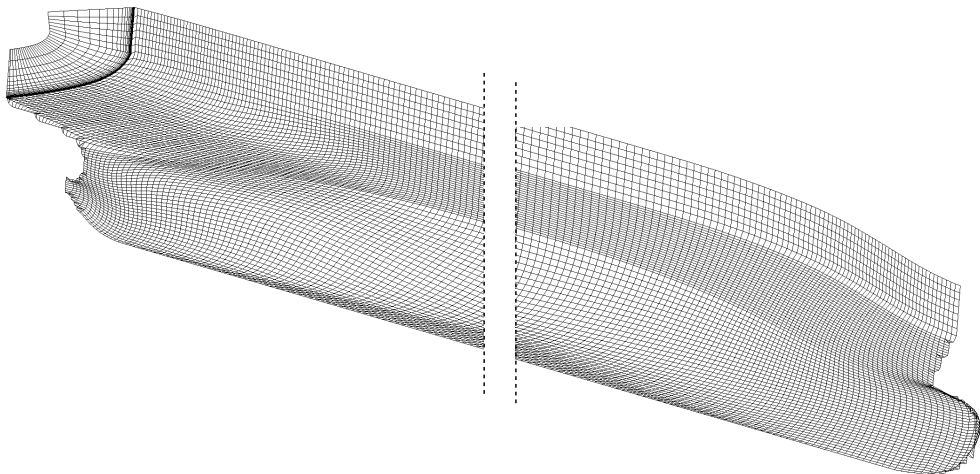


Figure 35: Surface grid on hull with visible fine region near free surface level, bow and stern part.

A sequence of six geometrically similar grids is generated for the grid dependence study. The number of cells varies from 0.35 to 7.88 million, see Table 6. The computations are carried out with Superbee discretization scheme.

Grid	Cells (1e6)	h/h_i ($i=1, 2, \dots, 7$)
G1	7.88	1.000
G2	2.78	1.414
G3	1.65	1.682
G4	0.98	2.000
G5	0.58	2.378
G6	0.35	2.828

Table 6: Grid sequence for the KCS hull.

5.4.2 Results – resistance

Similarly to the previous test case the grid convergence is investigated using the Least Squares Root approach. The measured resistance coefficient is presented together with the results obtained with the code in Table 7. The total resistance coefficient extrapolated to zero grid size shows a deviation from the measurements of about 2.5%.

Exp.	G0	G1	G2	G3	G4	G5	G6	
C _F	-	2.83	2.77	2.71	2.65	2.60	2.45	2.31
C _P	-	0.65	0.75	0.62	0.63	0.89	0.84	0.83
C _T	3.56	3.47	3.52	3.33	3.28	3.49	3.29	3.15

Table 7: Measured and computed results including values extrapolated to zero cell size. (All results multiplied by 1000.)

The grid convergence is monotonic and the observed order of accuracy, p , is 2.42. Table 8 summarizes the results of the uncertainty analysis. Figure 36 illustrates the grid convergence with a least square fit curve. A noticeable, but not unusual, scatter (Larsson and Zou (2010)) can be noticed for the pressure component which also affects the total resistance coefficient. The scatter that can be measured as a standard deviation of the data fit with the least square method contributes to about 50% of the numerical error of the total resistance coefficient.

F_n	$E\%$	$\varepsilon_{12}\%$	p	$U_I\%$	$U_{SN}\%$
0.260	1.01	5.67	2.42	0.92	6.96

Table 8: Results of uncertainty analysis for C_T .

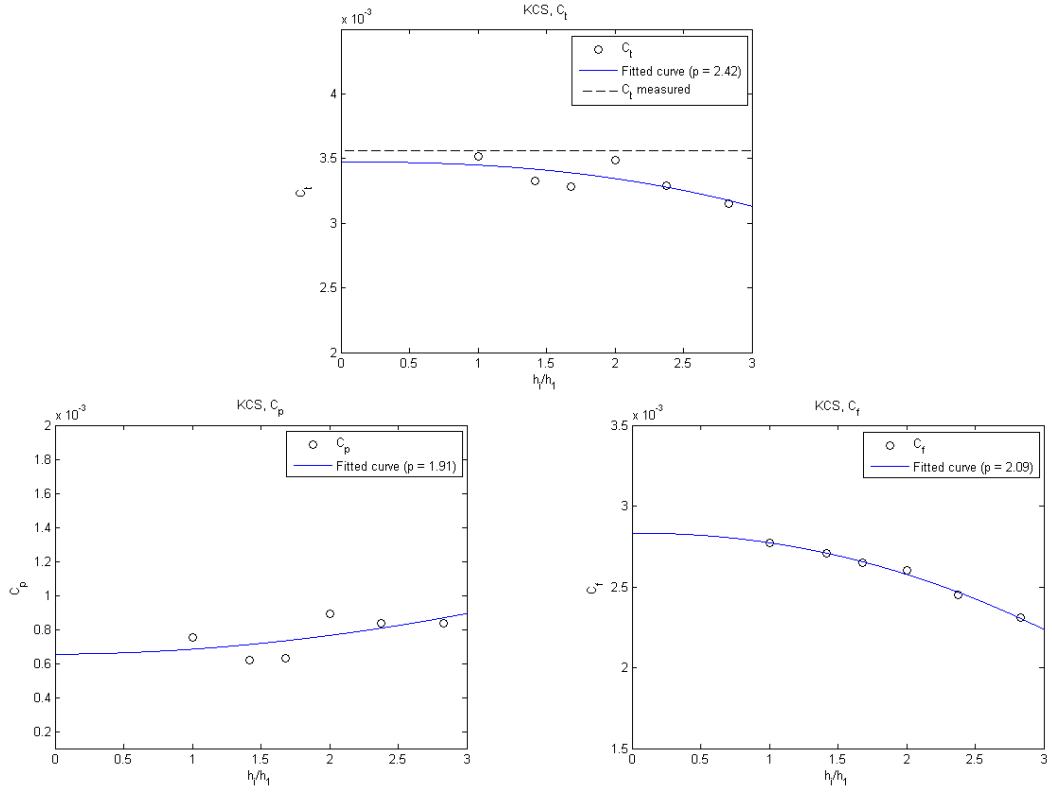


Figure 36: Grid convergence of C_T , C_P and C_F

5.4.3 Results – wave pattern

The computed free surface was compared to the measurements. The wave profile along the hull is presented in Figure 37. Apparently the predicted profile follows the measured one well. The largest deviations are at the bow and stern, where a thin film of the water is very difficult to predict. The bow wave crest is underestimated while the trough at the aft shoulder and the crest at the stern are slightly overestimated. The wave cuts show a very good correspondence with the measurements. Figures 38, 39 and 40 illustrate the cuts at y/L_{PP} of -0.074, -0.102 and -0.151. Analysis of the wave pattern indicates that all major features are represented well in the computations and that the pattern in general corresponds well with the measurements, see Figure 41. In the regions far from the hull, where the grid is coarsened rapidly, the waves are damped noticeably and lose their details. This can be mostly observed for the diverging and transverse waves behind the stern.

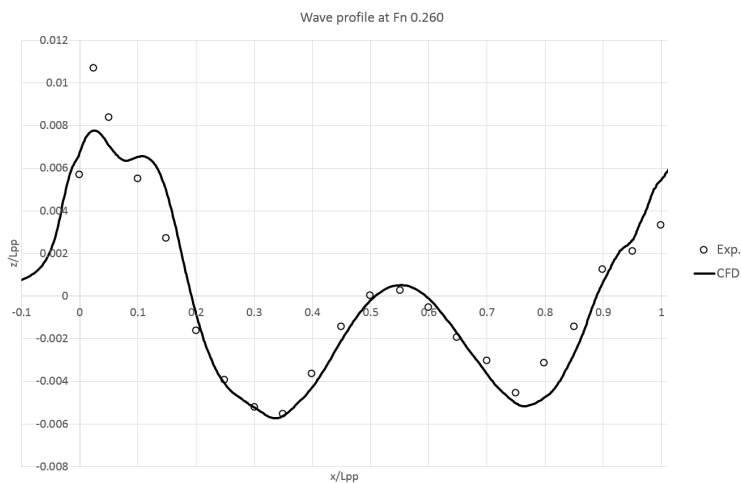


Figure 37: Computed and measured wave profile.

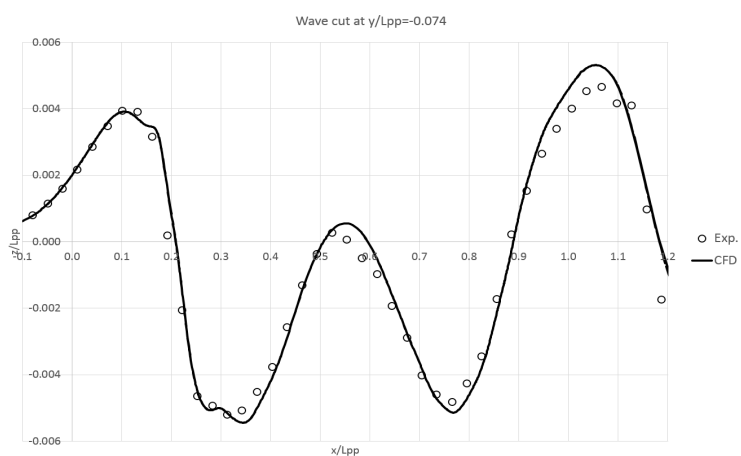


Figure 38: Computed and measured wave cut at $y/Lpp = -0.074$.

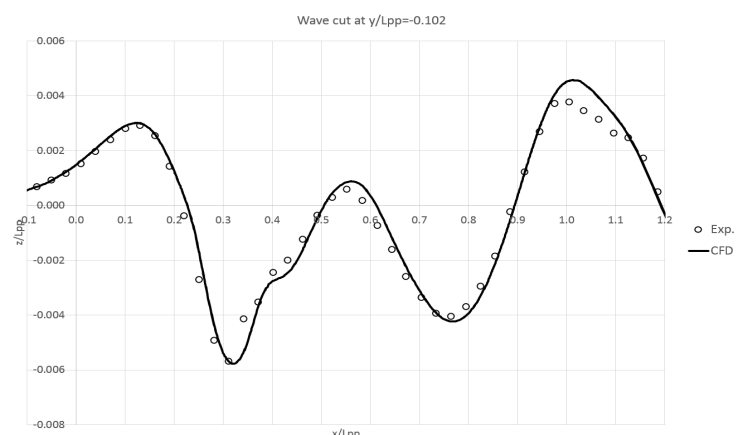


Figure 39: Computed and measured wave cut at $y/Lpp = -0.102$.

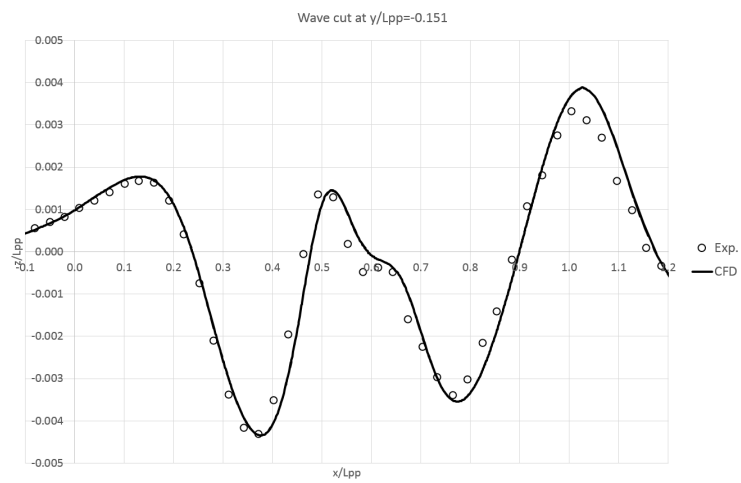


Figure 40: Computed and measured wave cut at $y/Lpp = -0.151$.

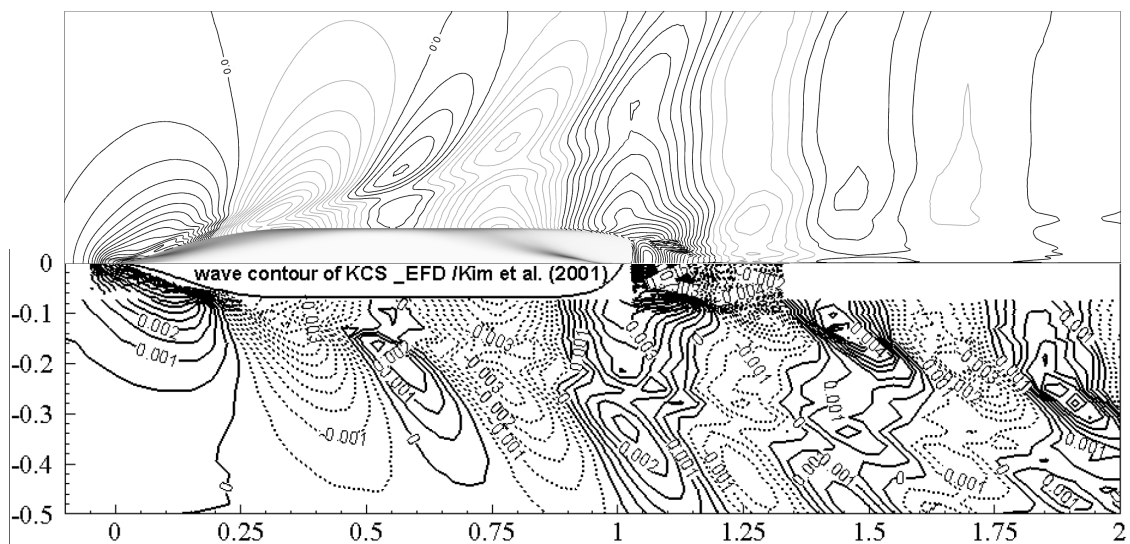


Figure 41: Computed (top) and measured (bottom) wave pattern, contour spacing 0.0005.

6 CONCLUSIONS AND FUTURE WORK

A free surface modeling has been implemented in an existing finite volume RANS code. A void fraction transport equation is solved together with momentum and continuity equations in a coupled manner. The Roe flux splitting with a defect correction is used for the convective flux discretization.

Several discretization schemes for the void fraction equation were tested on two test cases. It was found that the scheme has little effect on the wave profiles near the wave generating body, while the waves further away were more damped when a non-compressive scheme is used. However, the interface thickness reduction achievable with the compressive schemes had a great importance on the wave details and it was required to properly resolve for example a wave crest, e.g. near the bow.

Due to the refinement application it was possible to reduce numerical diffusion using smaller cells close to the interface. Further improvement was achieved by the adaptation method that makes the cells parallel to the interface. The results showed that it was possible to keep the interface sharp with a limited number of additional cells. The cell face alignment with the interface improved the sharpness for the relatively diffusive discretization scheme applied for this calculation. It was also found that the method for interpolation of the water fraction field had to be modified at the upstream boundary of the refinement. This was to reduce the interface thickness convected into the refinement from the coarse upstream background grid.

The simulations of a submerged hydrofoil case showed reasonably good agreement with the experimental data. Very little wave damping could be seen and the interface was sharp. The simulations of the Series 60 test case gave satisfactory results despite a rather coarse grid. The wave pattern was in good agreement with the measurements and the numerical damping was visible mostly in the coarse grid region away from the ship. The grid dependence study carried out on the Wigley and KCS hulls showed the robustness of the code and its capability to accurately predict ship resistance.

Based on the experience gained during the work the following important conclusions can be drawn. The adaptive refinements following the wave profiles can be difficult to handle in case of wave breaking. The comparison of the results with the fixed and adaptive grids for various discretization methods indicate that with a well suited compressive scheme the interface thickness does not become smaller when the adaptation is used. Therefore, more important than the adaptivity is the discretization scheme itself and the local refinement, even if it is fixed. The further work should address grid quality which was not discussed here but the importance of it should not be underestimated. Apart from introducing a dynamic sinkage and trim more effort should be put into improving convergence rate and validation of both low and high Froude number cases.

REFERENCES

- BROBERG, L., REGNSTRÖM, B., ÖSTBERG, M. (2007): *XCHAP – Theoretical Manual*, FLOWTECH International AB.
- CARRICA, P.M., WILSON,R.,V. and STERN, F. (2005): *Free surface flows around ships: Progress towards simulation of high-speed flows and motions*, Mecanica Computational Vol. XXIV, A. Larreteguy (Editor), Buenos Aires, Argentina
- CHAKRAVARTHY, S. & OSHER, S. (1985): *A New Class of High Accuracy TVD Schemes for Hyperbolic Conservation Laws*, AIAA paper-85-0363.
- DARWISH, M., Moukalled, F. (2006): *Convective Schemes for Capturing Interfaces of Free-Surface Flows on Unstructured Grids*, Numerical Heat Transfer, Part B, 49: 19–42
- DICK, E., LINDEN, J. (1992): *A Multigrid Method for Steady Incompressible Navier-Stokes Equations Based on Flux Difference Splitting*, International Journal for Numerical Methods in Fluids, Vol.14, 1311-1323.
- DUNCAN, J. H. (1983), *The breaking and non-breaking wave resistance of a two-dimensional hydrofoil*, J. Fluid Mechanics, Vol. 126, pp. 507-520.
- EÇA, L., HOEKSTRA, M., (2006): *Discretization Uncertainty Estimation Based on a Least Squares Version of the Grid Convergence Index*, Proceedings of the 2nd Workshop onCFD Uncertainty Analysis, Lisbon, Portugal
- FROMM, J.M. (1968): *A method for reducing dispersion in convective difference schemes*, Journal of Computational Physics, 3, 176-189
- GASKELL, P. H., LAU, A. K. C. (1988): *Curvature-compensated convective transport: SMART, a new boundedness-preserving transport algorithm*, Int. J. Num. Meth. Fluids, 8, p617.
- HARTEN, A. (1997): *High Resolution Schemes for Hyperbolic Conservation Laws*, Journal of Computational Physics, 135, 260-278.
- HAY, A., VISONNEAU M. (2005): *Computation of free-surface flows with local mesh adaptation*, International Journal for Numerical Methods in Fluids, Volume 49 Issue 7, Pages 785 – 816
- HENSHAW, W. (1994): *A fourth-order accurate method for the incompressible Navier-Stokes equations on overlapping grids*, J. Comp. Phys., 113, pp. 13–25.
- JANSON, C-E. (1997): *Potential Flow Panel Methods for the Calculation of Free-surface Flows with Lift*, PhD Thesis, Chalmers University of Technology, Göteborg, Sweden
- JENSEN, G., BERTRAM, V., SÖDING, H. (1989): *Ship Wave-Resistance Computations*. Proceedings of the 5th International Conference on Numerical Ship Hydrodynamics, Hiroshima, Japan.
- KAJITANI, H. ; MIYATA, H. ; IKEHATA, M. ; TANAKA, H. ; ADACHI, H. ; NAMIMATSU, M. ; OGAWARA, S. (1983): *The Summary of the Cooperative Experiment on Wigley Parabolic Model in Japan*. Proceedings of The 2nd

DTNSTDC Workshop on Ship Wave-Resistance Computations, Bethesda, Maryland, USA.

LARSSON, L., RAVEN, H., C. (2010): *The Principles of Naval Architecture Series: Ship Resistance and Flow*. The Society of Naval Architects and Marine Engineers, USA

LARSSON, L., ZOU, L. (2013): *Evaluation of Resistance, Sinkage and Trim, Self-Propulsion and Wave Pattern Predictions in Numerical Ship Hydrodynamics – An Assessment of the Gothenburg 2010 Workshop* by L. Larsson, F. Stern and M. Visonneau (eds.), Springer Science and Business Media, Dordrecht

LEONARD, B. P. (1991): *The ULTIMATE conservative difference scheme applied to unsteady one-dimensional advection*. Computer Methods in Applied Mechanics and Engineering, 88, 17-74.

LEVEQUE, R. J. (1998): *Balancing Source Terms and Flux Gradients in High-Resolution Godunov Methods: The Quasi-Steady Wave-Propagation Algorithm*. Journal of Computational Physics, 146, 346-365.

MENTER, F.R. (1993): *Zonal Two Equation k-w Turbulence Models for Aerodynamic Flows*, 24th Fluid Dynamics Conference, Orlando, AIAA paper-93-2906.

MUZAFERIJA S., PERIC M. (1998): *Computation of free-surface flows using interface-tracking and interface-capturing methods*, in Mahrenholz O, Markiewicz M. (eds.), Nonlinear Water Wave Interaction, Computational Mechanics Publications, Southampton

NAKAHASHI, K., TOGASHI, F., SHAROV, D. (2000): *Intergrid-Boundary Definition Method for Overset Unstructured Grid Approach*, AIAA JOURNAL Vol. 38, No. 11

NOACK, R. (2005): *SUGGAR: a General Capability for Moving Body Overset Grid Assembly*, 17th AIAA Computational Fluid Dynamics Conf., Toronto, Ontario, Canada

ORYCH, M., REGNSTRÖM, B., LARSSON, L. (2009): *A Surface Capturing Method in the RANS Solver SHIPFLOW*. 12th Numerical Towing Tank Symposium, Cortona, Italy 4-6 October 2009.

RAVEN, H., C. (1992): *A Practical Nonlinear Method for Calculating Ship Wavemaking and Wave Resistance*, 19th Symposium on Naval Hydrodynamics, Seoul, Korea.

REGNSTRÖM, B., BROBERG, L. AND LARSSON, L. (2000): *Ship Stern Flow Calculations on Overlapping Composite Grids*, 23rd ONR Symp. Naval Hydrodynamics, Val de Reuil, France

REGNSTRÖM, B. (2007), *Introduction to overlapping grids in SHIPFLOW*, FLOWTECH International AB

ROE, P. L. (1997): *Approximate Riemann Solvers, Parameter Vectors, and Difference Schemes*, Journal of Computational Physics, Vol. 135, No. 2, pp. 250-258.

STEGER, J. L., DOUGHERTY, F. C. and BENEK, J. A. (1983): *A Chimera Grid*

Scheme, Advances in Grid Generation, K. N. Ghia and U. Ghia, eds., ASME FED-Vol. 5, June, 1983.

SWEBY, P. K. (1984): *High Resolution Schemes Using Flux Limiters for Hyperbolic Conservation Laws*. SIAM J Numer Anal, 21, 995-1011.

TODA, Y., STERN, F., LONGO, J. (1992): *Mean-Flow Measurements in the Boundary Layer and Wake and Wave Field of a Series 60 CB=0.6 Ship Model – Part 1: Froude Numbers 0.16 and 0.316*. Journal of Ship Research, Vol. 36, No. 4, pp. 360-377.

UBBINK, O., ISSA, R. (1999): *A Method for Capturing Sharp Fluid Interfaces on Arbitrary Meshes*. J. Comput. Phys., vol. 153, pp. 26–50.

Van LEER, B. (1979): *Towards the ultimate conservative difference scheme, V. A second order sequel to Godunov's method*. J. Comp. Phys., 32, p101.

VERSTEG, H. K., MALALASEKERA, W. (1995): *An Introduction to Computational Fluid Dynamics*, Longman Scientific & Technical, Essex, England.

WACKERS, J. (2007), *Surface capturing and multigrid for steady free-surface water flows*, PhD Thesis, Technische Universiteit Delft.

WATERSON, N.P., DECONINCK H. (2007): *Design principles for bounded higher-order convection schemes – a unified approach*. Journal of Computational Physics, Vol. 224, pp. 182-207.

ZOU, L., LARSSON, L. (2013): *A Verification and Validation Study Based on Resistance Submissions to the Gothenburg 2010 Workshop on Numerical Ship Hydrodynamics*, in *Numerical Ship Hydrodynamics – An Assessment of the Gothenburg 2010 Workshop* by L. Larsson, F. Stern and M. Visonneau (eds.), Springer Science and Business Media, Dordrecht